

MIT Open Access Articles

A thermo-mechanically coupled theory for large deformations of amorphous polymers. Part II: Applications

The MIT Faculty has made this article openly available. **Please share** how this access benefits you. Your story matters.

Citation: Ames, Nicoli M. et al. "A Thermo-mechanically Coupled Theory for Large Deformations of Amorphous Polymers. Part II: Applications." *International Journal of Plasticity* 25.8 (2009) : 1495-1539.

As Published: <http://dx.doi.org/10.1016/j.ijplas.2008.11.005>

Publisher: Elsevier B.V.

Persistent URL: <http://hdl.handle.net/1721.1/65576>

Version: Author's final manuscript: final author's manuscript post peer review, without publisher's formatting or copy editing

Terms of Use: Article is made available in accordance with the publisher's policy and may be subject to US copyright law. Please refer to the publisher's site for terms of use.



A thermo-mechanically-coupled theory for large deformations of amorphous polymers. Part II: applications

Nicoli M. Ames, Vikas Srivastava, Shawn A. Chester, and Lallit Anand*
Department of Mechanical Engineering
Massachusetts Institute of Technology
Cambridge, MA 02139, USA

Abstract

We have conducted large strain compression experiments on three representative amorphous polymeric materials: poly(methyl methacrylate) (PMMA), polycarbonate (PC), and a cyclo-olefin polymer (Zeonex-690R), in a temperature range spanning room temperature to slightly below the glass transition temperature of each material, in a strain rate range of $\approx 10^{-4} \text{ s}^{-1}$ to 10^{-1} s^{-1} , and compressive true strains exceeding 100%.

The constitutive theory developed in Part I (Anand et al., 2008) is specialized to capture the salient features of the thermo-mechanically-coupled strain rate and temperature dependent large deformation mechanical response of amorphous polymers. For the three amorphous polymers studied experimentally, the specialized constitutive model is shown to perform well in reproducing the following major intrinsic features of the macroscopic stress-strain response of these materials: (a) the strain rate and temperature dependent yield strength; (b) the transient yield-peak and strain-softening which occurs due to deformation-induced disordering; (c) the subsequent rapid strain-hardening due to alignment of the polymer chains at large strains; (d) the unloading response at large strains; and (e) the temperature rise due to plastic-dissipation and the limited time for heat-conduction for the compression experiments performed at strain rates $\gtrsim 0.01 \text{ s}^{-1}$.

We have implemented our thermo-mechanically-coupled constitutive model by writing a user material subroutine for the finite element program ABAQUS/Explicit (2007).

In order to validate the predictive capabilities of our constitutive theory and its numerical implementation, we have performed the following validation experiments: (i) isothermal fixed-end large-strain reversed-torsion tests on PC; (ii) macroscale isothermal plane-strain cold- and hot-forming operations on PC; (iii) macroscale isothermal, axi-symmetric hot-forming operations on Zeonex; (iv) macroscale hot-embossing of Zeonex; and (v) high-speed normal-impact of a circular plate of PC with a spherical-tipped cylindrical projectile. By comparing the results from this suite of validation experiments of some key macroscopic features, such as the experimentally measured deformed shapes and the load-displacement curves, against corresponding results from numerical simulations, we show that our theory is capable of reasonably accurately reproducing the experimental results obtained in the validation experiments.

1 Introduction

This, Part II of our two-part paper, is devoted to applications of the theory developed in Part I (Anand et al., 2008).

The plan of the paper is as follows. In §2 we briefly describe our experiments on three representative amorphous polymeric materials: poly(methyl methacrylate) (PMMA), polycarbonate (PC), and a cyclo-olefin polymer (Zeonex-690R),¹ in a temperature range spanning room temperature to slightly below the glass

*Corresponding author. Tel.: +1-617-253-1635; E-mail address: anand@mit.edu

¹From Zeon Chemicals; henceforth, simply called Zeonex in this paper. Relative to PMMA and PC, Zeonex is biocompatible, has lower moisture uptake, has better light-transmittance characteristics, and it is also chemically-resistant to a wider variety of solvents.

transition temperature of each material, in a strain rate range of $\approx 10^{-4} \text{ s}^{-1}$ to 10^{-1} s^{-1} , and compressive true strains exceeding 100%. In §3 we summarize the major aspects of the general constitutive theory outlined in Part I (Anand et al., 2008). Then in §4 we specialize this constitutive theory to capture the salient features of the experimentally-measured mechanical response of PMMA, PC and Zeonex. In an Appendix, §8, we describe in reasonable detail our heuristic method to calibrate the material parameters/functions appearing in our constitutive theory. The quality of the fit of the specialized model to the experimentally-measured stress-strain curves is discussed in §5, where we show that for the three amorphous polymers studied experimentally, the constitutive model performs well in reproducing the following major intrinsic features of the macroscopic stress-strain response of these materials: (a) the strain rate and temperature dependent yield strength; (b) the transient yield-peak and strain-softening which occurs due to deformation-induced disordering; (c) the subsequent rapid strain-hardening due to alignment of the polymer chains at large strains; (d) the unloading response at large strains; and (e) the temperature rise due to plastic-dissipation and the limited time for heat-conduction for the compression experiments performed at strain rates $\gtrsim 0.01 \text{ s}^{-1}$.

We have implemented our thermo-mechanically-coupled constitutive model by writing a user material subroutine for the finite element program ABAQUS/Explicit (2007). In §6, we present results of a suite of experiments that we have conducted in order to validate the predictive capabilities of our constitutive theory and its numerical implementation. By comparing the results of some key macroscopic features from this set of validation experiments, such as the experimentally measured deformed shapes and the load-displacement curves, against corresponding results from numerical simulations, we show that our theory is capable of reasonably accurately reproducing the experimental results obtained in the validation experiments. We close in §7 with some final remarks.

2 Simple compression experiments on three different amorphous polymers

We have conducted a suite of simple compression experiments on three technologically important amorphous polymers: poly(methyl methacrylate) (PMMA), polycarbonate (PC), and a cyclo-olefin polymer (Zeonex-690R). The nominal glass transition temperatures, ϑ_g , of these three materials are:

$$\text{PMMA: } \vartheta_g \approx 115 \text{ C}, \quad \text{PC: } \vartheta_g \approx 145 \text{ C}, \quad \text{and} \quad \text{Zeonex-690R: } \vartheta_g \approx 135 \text{ C}.$$

The cylindrical compression test specimens were 12.7 mm diameter and 12.7 mm tall, and were annealed before and after machining to final shape by heating in a furnace at a temperature about 10 C above the glass transition temperature of each material, and holding at that temperature for two hours, before cooling to room temperature.² The experiments were conducted using a servo-hydraulic Instron testing machine, fitted with a high-temperature furnace. Amorphous polymers are poor thermal conductors; accordingly, in order to heat the compression specimens uniformly, we also used heated steel compression platens in addition to the furnace. The platens were heated with cartridge heaters, and thermocouples inserted into each platen were used to control the temperature. The top compression platen also had an integrated spherical seat to help minimize any effects of misalignment during compression testing. To reduce friction at the platen/specimen interface, the platens were polished, and thin Teflon (PTFE) films were used as lubricating layers between the specimen and the platens.³ Before a given experiment, each specimen was allowed to anneal at the testing temperature for one hour prior to testing. Experiments on PMMA were conducted for the temperature range 25 C to 110 C at four strain-rates: 3×10^{-4} , 10^{-3} , 10^{-2} , and 10^{-1} s^{-1} . On PC the experiments were conducted for the temperature range 25 C to 130 C at three strain-rates: 10^{-3} , 10^{-2} , and 10^{-1} s^{-1} . While on Zeonex the experiments were conducted for the temperature range 25 C to 130 C at four strain-rates: 3×10^{-4} , 3×10^{-3} , 3×10^{-2} , and $3 \times 10^{-1} \text{ s}^{-1}$. The compression tests were carried out at constant *true strain-rates* to compressive true strains exceeding $\gtrsim 100\%$; all strain measurements were made using an extensometer.

²After annealing, the PMMA and PC specimens were slowly cooled in the furnace to room temperature over a period of several hours, while the Zeonex was quenched in water.

³For true strains up to 100% our compression specimens showed very little or no bulging; however, for larger strain levels, in spite of our precautions to minimize friction, some bulging did occur.

Fig. 1 shows representative stress-strain curves for PMMA at strain-rate of $3 \times 10^{-4} \text{ s}^{-1}$ at temperatures ranging from 25 C through 110 C, while Fig. 2 shows a more extensive set of stress-strain curves for strain rates of 3×10^{-4} , 10^{-3} , 10^{-2} , and 10^{-1} s^{-1} and temperatures of 25 C through 110 C.⁴ Referring to Fig. 1, we see that as the temperature increases in the glassy region, from 25 C to 110 C, the yield strength decreases by an order of magnitude from $\approx 100 \text{ MPa}$ to $\approx 10 \text{ MPa}$, and the strain-hardening observed at large strains due to limited extensibility of the polymer chains diminishes. Referring to Fig. 2, which shows stress-strain curves at various fixed temperatures and the four different strain rates, we see obvious strain-rate dependent features of the material response. In the low-temperature glassy region, the yield strength of the material increases by about 10% for a one-decade increase in strain-rate at any given temperature. Another important strain rate dependent feature is the softening observed at large strains at the two higher strain rates of 10^{-2} and 10^{-1} s^{-1} at temperatures of 25 C, 50 C and 70 C. The softening is attributable to (near) “adiabatic” heating at the higher strain rates. While we did not measure the actual temperature rise in our specimens, Arruda et al. (1995) have shown that the surface temperature of a compression specimen, for a test carried out at 20 C, could increase by as much $\approx 20 \text{ C}$ after a 100% compressive strain at a strain rate of 10^{-1} s^{-1} .

Stress-strain curves for PC and Zeonex will be presented in §5, where we compare experimental stress-strain curves against those resulting from our constitutive model. In the next section §3 we summarize the theory developed in Part I; in §4, we specialize the theory for applications; and then in §5 we show results of the fit of the specialized constitutive theory to the data from our experiments on PMMA, PC, and Zeonex.

3 Theory

We begin by recalling the theory for isotropic elastic viscoplastic materials developed in Part I of this paper (Anand et al., 2008). The theory relates the following basic fields:⁵

$\mathbf{x} = \chi(\mathbf{X}, t)$,	motion;
$\mathbf{F} = \nabla \chi$, $J = \det \mathbf{F} > 0$,	deformation gradient;
$\mathbf{F} = \mathbf{F}^e \mathbf{F}^p$,	elastic-plastic decomposition of \mathbf{F} ;
\mathbf{F}^e , $J^e = \det \mathbf{F}^e = J > 0$,	elastic distortion;
\mathbf{F}^p , $J^p = \det \mathbf{F}^p = 1$,	inelastic distortion;
$\mathbf{F} = \mathbf{R}\mathbf{U} = \mathbf{V}\mathbf{R}$,	polar decomposition of \mathbf{F} ;
$\mathbf{F}^e = \mathbf{R}^e \mathbf{U}^e = \mathbf{V}^e \mathbf{R}^e$,	polar decomposition of \mathbf{F}^e ;
$\mathbf{F}^p = \mathbf{R}^p \mathbf{U}^p = \mathbf{V}^p \mathbf{R}^p$,	polar decomposition of \mathbf{F}^p ;
$\mathbf{C} = \mathbf{F}^\top \mathbf{F}$, $\mathbf{B} = \mathbf{F}\mathbf{F}^\top$,	right and left Cauchy-Green tensors;
$\mathbf{C}^e = \mathbf{F}^{e\top} \mathbf{F}^e$, $\mathbf{B}^e = \mathbf{F}^e \mathbf{F}^{e\top}$,	elastic right and left Cauchy-Green tensors;
$\mathbf{C}^p = \mathbf{F}^{p\top} \mathbf{F}^p$, $\mathbf{B}^p = \mathbf{F}^p \mathbf{F}^{p\top}$,	plastic right and left Cauchy-Green tensors;
$\mathbf{T} = \mathbf{T}^\top$,	Cauchy stress;
$\mathbf{T}_R = J \mathbf{T} \mathbf{F}^{-\top}$,	Piola stress;
ψ_R ,	free energy density per unit reference volume;
$\boldsymbol{\xi} = (\xi_1, \xi_2, \dots, \xi_m)$	m scalar internal variables;
\mathbf{A} , $\mathbf{A} = \mathbf{A}^\top$, $\det \mathbf{A} = 1$	tensorial internal variable;
$\vartheta > 0$,	absolute temperature;
$\nabla \vartheta$,	referential temperature gradient;
\mathbf{q}_R ,	referential heat flux vector.

⁴As is customary, in order to calculate the deformed cross-sectional area (and thence the true stress), we have assumed plastic incompressibility to estimate the stretch in the lateral direction of the compression specimens.

⁵Notation: We use standard notation of modern continuum mechanics. Specifically: ∇ and Div denote the gradient and divergence with respect to the material point \mathbf{X} in the reference configuration; grad and div denote these operators with respect to the point $\mathbf{x} = \chi(\mathbf{X}, t)$ in the deformed body; a superposed dot denotes the material time-derivative. Throughout, we write $\mathbf{F}^{e-1} = (\mathbf{F}^e)^{-1}$, $\mathbf{F}^{p-\top} = (\mathbf{F}^p)^{-\top}$, etc. We write $\text{tr} \mathbf{A}$, $\text{sym} \mathbf{A}$, $\text{skw} \mathbf{A}$, \mathbf{A}_0 , and $\text{sym}_0 \mathbf{A}$ respectively, for the trace, symmetric, skew, deviatoric, and symmetric-deviatoric parts of a tensor \mathbf{A} . Also, the inner product of tensors \mathbf{A} and \mathbf{B} is denoted by $\mathbf{A} : \mathbf{B}$, and the magnitude of \mathbf{A} by $|\mathbf{A}| = \sqrt{\mathbf{A} : \mathbf{A}}$.

3.1 Constitutive equations

1. Free energy

The free energy is given by

$$\psi_{\text{R}} = \tilde{\psi}^{(1)}(\mathcal{I}_{\mathbf{C}^e}, \vartheta) + \tilde{\psi}^{(2)}(\mathcal{I}_{\mathbf{C}}, \vartheta) + \tilde{\psi}^{(p)}(\mathcal{I}_{\mathbf{A}}, \vartheta), \quad (3.1)$$

where $\mathcal{I}_{\mathbf{C}^e}$, $\mathcal{I}_{\mathbf{C}}$, and $\mathcal{I}_{\mathbf{A}}$ are the lists of the principal invariants of \mathbf{C}^e , \mathbf{C} , and \mathbf{A} , respectively. In (3.1), $\tilde{\psi}^{(1)}$ is an energy associated with intermolecular interactions and modeled using the elastic Cauchy-Green tensor \mathbf{C}^e ; $\tilde{\psi}^{(2)}$ is an energy associated with the stretching of the polymer chains and modeled using the total Cauchy-Green tensor \mathbf{C} ; and $\tilde{\psi}^{(p)}$ is an energy associated with plastic deformation, and assumed to depend on the internal variable \mathbf{A} . This last “defect energy” leads to the development of a *back-stress*, and allows one to phenomenologically account for Bauschinger-like phenomena; in addition, it contributes in an important manner to the plastic source term in the balance of energy.

2. Cauchy stress

The Cauchy stress is given by

$$\mathbf{T} = \mathbf{T}^{(1)} + \mathbf{T}^{(2)}, \quad (3.2)$$

where

$$\mathbf{T}^{(1)} \stackrel{\text{def}}{=} J^{-1} \left(\mathbf{F}^e \mathbf{S}^e \mathbf{F}^{e\tau} \right), \quad \text{with} \quad \mathbf{S}^e = 2 \frac{\partial \tilde{\psi}^{(1)}(\mathcal{I}_{\mathbf{C}^e}, \vartheta)}{\partial \mathbf{C}^e}, \quad (3.3)$$

and

$$\mathbf{T}^{(2)} \stackrel{\text{def}}{=} J^{-1} \left(\mathbf{F} \mathbf{S} \mathbf{F}^\tau \right), \quad \text{with} \quad \mathbf{S} = 2 \frac{\partial \tilde{\psi}^{(2)}(\mathcal{I}_{\mathbf{C}}, \vartheta)}{\partial \mathbf{C}}. \quad (3.4)$$

3. Driving stresses for plastic flow

With

$$\mathbf{M}^e = \mathbf{C}^e \mathbf{S}^e, \quad (3.5)$$

denoting a *symmetric* Mandel stress,

$$\mathbf{M}_{\text{back}} = 2 \left(\frac{\partial \tilde{\psi}^{(p)}(\mathcal{I}_{\mathbf{A}}, \vartheta)}{\partial \mathbf{A}} \mathbf{A} \right)_0, \quad (3.6)$$

a *symmetric and deviatoric* back-stress, and

$$\mathbf{M}_{\text{eff}}^e = \mathbf{M}^e - \mathbf{M}_{\text{back}} \quad (3.7)$$

an *effective Mandel stress*, the driving stress for plastic flow is taken as the stress difference

$$(\mathbf{M}_{\text{eff}}^e)_0 = \mathbf{M}_0^e - \mathbf{M}_{\text{back}}. \quad (3.8)$$

4. Flow rule

The evolution equation for \mathbf{F}^p is

$$\dot{\mathbf{F}}^p = \mathbf{D}^p \mathbf{F}^p, \quad (3.9)$$

with \mathbf{D}^p given by

$$\mathbf{D}^p = d^p \mathbf{N}^p, \quad \mathbf{N}^p = \frac{(\mathbf{M}_{\text{eff}}^e)_0}{|(\mathbf{M}_{\text{eff}}^e)_0|}, \quad (3.10)$$

where with

$$\mathbf{\Lambda} \stackrel{\text{def}}{=} \{ \mathbf{C}^e, \mathbf{B}^p, \mathbf{A}, \boldsymbol{\xi}, \vartheta \} \quad (3.11)$$

denoting a list of constitutive variables, the scalar flow rate d^p is obtained by solving the scalar strength relation

$$|(\mathbf{M}_{\text{eff}}^e)_0| = Y(d^p, \mathbf{\Lambda}), \quad (3.12)$$

for given $(\mathbf{M}_{\text{eff}}^e)_0$ and $\mathbf{\Lambda}$, where $Y(d^p, \mathbf{\Lambda})$ is the strength function, which is an isotropic function of its arguments.

5. Evolution equations for internal variables

The internal variables $\boldsymbol{\xi}$ and \mathbf{A} are presumed to evolve according to the differential equations

$$\left. \begin{aligned} \dot{\xi}_i &= h_i(d^p, \boldsymbol{\Lambda}), \\ \dot{\mathbf{A}} &= \mathbf{D}^p \mathbf{A} + \mathbf{A} \mathbf{D}^p - \mathbf{G}(\boldsymbol{\Lambda}) d^p, \end{aligned} \right\} \quad (3.13)$$

with the functions h_i and \mathbf{G} isotropic functions of their arguments, and since \mathbf{A} is unimodular, the function \mathbf{G} must satisfy $\text{tr}(\mathbf{G}\mathbf{A}^{-1}) = 0$.

6. Fourier's Law

The heat flux is taken to be given by Fourier's law

$$\mathbf{q}_R = -\kappa \nabla \vartheta, \quad (3.14)$$

with $\kappa(\vartheta) > 0$ the thermal conductivity.

The evolution equations for \mathbf{F}^p , $\boldsymbol{\xi}$ and \mathbf{A} need to be accompanied by initial conditions. Typical initial conditions presume that the body is initially (at time $t = 0$, say) in a **virgin state** in the sense that

$$\mathbf{F}(\mathbf{X}, 0) = \mathbf{F}^p(\mathbf{X}, 0) = \mathbf{A}(\mathbf{X}, 0) = \mathbf{1}, \quad \xi_i(\mathbf{X}, 0) = \xi_{i0} \quad (= \text{constant}), \quad (3.15)$$

so that by $\mathbf{F} = \mathbf{F}^e \mathbf{F}^p$ we also have $\mathbf{F}^e(\mathbf{X}, 0) = \mathbf{1}$.

3.2 Partial differential equations for the deformation and temperature fields

The partial differential equation for the deformation is obtained from the local force balance

$$\text{Div} \mathbf{T}_R + \mathbf{b}_{0R} = \rho_R \ddot{\boldsymbol{\chi}}, \quad (3.16)$$

where $\mathbf{T}_R = J \mathbf{T} \mathbf{F}^{-T}$ is the Piola stress, \mathbf{b}_{0R} is the non-inertial body force, ρ_R is the mass density in the reference body, and $\ddot{\boldsymbol{\chi}}$ is the acceleration.

Balance of energy gives the following partial differential equation for the temperature

$$\begin{aligned} c \dot{\vartheta} &= -\text{Div} \mathbf{q}_R + q_R + \left(|(\mathbf{M}_{\text{eff}}^e)_0| + \left(\frac{\partial \tilde{\psi}^{(p)}(\mathcal{I}_{\mathbf{A}}, \vartheta)}{\partial \mathbf{A}} : \mathbf{G}(\boldsymbol{\Lambda}) \right) \right) d^p \\ &+ \frac{1}{2} \vartheta \frac{\partial \mathbf{S}^e}{\partial \vartheta} : \dot{\mathbf{C}}^e + \frac{1}{2} \vartheta \frac{\partial \mathbf{S}}{\partial \vartheta} : \dot{\mathbf{C}} + \vartheta \frac{\partial^2 \tilde{\psi}^{(p)}(\mathcal{I}_{\mathbf{A}}, \vartheta)}{\partial \vartheta \partial \mathbf{A}} : \dot{\mathbf{A}}, \end{aligned} \quad (3.17)$$

where the specific heat in the theory is given by

$$c \stackrel{\text{def}}{=} -\vartheta \left(\frac{\partial^2 \tilde{\psi}^{(1)}(\mathcal{I}_{\mathbf{C}^e}, \vartheta)}{\partial \vartheta^2} + \frac{\partial^2 \tilde{\psi}^{(2)}(\mathcal{I}_{\mathbf{C}}, \vartheta)}{\partial \vartheta^2} + \frac{\partial^2 \tilde{\psi}^{(p)}(\mathcal{I}_{\mathbf{A}}, \vartheta)}{\partial \vartheta^2} \right). \quad (3.18)$$

4 Specialization of the constitutive equations

In this section, based on experience with existing recent theories of isotropic viscoplasticity of polymeric materials, we specialize the constitutive theory by imposing additional constitutive assumptions.

4.1 Free energy $\psi^{(1)}$

The spectral representation of \mathbf{C}^e is

$$\mathbf{C}^e = \sum_{i=1}^3 \omega_i^e \mathbf{r}_i^e \otimes \mathbf{r}_i^e, \quad \text{with} \quad \omega_i^e = \lambda_i^{e2}, \quad (4.1)$$

where $(\mathbf{r}_1^e, \mathbf{r}_2^e, \mathbf{r}_3^e)$ are the orthonormal eigenvectors of \mathbf{C}^e and \mathbf{U}^e , and $(\lambda_1^e, \lambda_2^e, \lambda_3^e)$ are the positive eigenvalues of \mathbf{U}^e . Instead of using the invariants $\mathcal{I}_{\mathbf{C}^e}$, the free energy $\psi^{(1)}$ for isotropic materials may be alternatively expressed in terms of the principal stretches and temperature as

$$\psi^{(1)} = \check{\psi}(\lambda_1^e, \lambda_2^e, \lambda_3^e, \vartheta). \quad (4.2)$$

Then, by the chain-rule and (3.3)₂, the stress \mathbf{S}^e is given by

$$\mathbf{S}^e = 2 \frac{\partial \check{\psi}^{(1)}(\lambda_1^e, \lambda_2^e, \lambda_3^e, \vartheta)}{\partial \mathbf{C}^e} = 2 \sum_{i=1}^3 \frac{\partial \check{\psi}^{(1)}(\lambda_1^e, \lambda_2^e, \lambda_3^e, \vartheta)}{\partial \lambda_i^e} \frac{\partial \lambda_i^e}{\partial \mathbf{C}^e} = \sum_{i=1}^3 \frac{1}{\lambda_i^e} \frac{\partial \check{\psi}^{(1)}(\lambda_1^e, \lambda_2^e, \lambda_3^e, \vartheta)}{\partial \lambda_i^e} \frac{\partial \omega_i}{\partial \mathbf{C}^e}. \quad (4.3)$$

Assume that the squared principal stretches ω_i^e are distinct, so that the ω_i^e and the principal directions \mathbf{r}_i^e may be considered as functions of \mathbf{C}^e ; then

$$\frac{\partial \omega_i^e}{\partial \mathbf{C}^e} = \mathbf{r}_i^e \otimes \mathbf{r}_i^e, \quad (4.4)$$

and, granted this, (4.4) and (4.3) imply that

$$\mathbf{S}^e = \sum_{i=1}^3 \frac{1}{\lambda_i^e} \frac{\partial \check{\psi}^{(1)}(\lambda_1^e, \lambda_2^e, \lambda_3^e, \vartheta)}{\partial \lambda_i^e} \mathbf{r}_i^e \otimes \mathbf{r}_i^e. \quad (4.5)$$

Further, from (3.3)₁,

$$\mathbf{T}^{(1)} = J^{-1} \mathbf{F}^e \mathbf{S}^e \mathbf{F}^{e\top} = J^{-1} \mathbf{R}^e \mathbf{U}^e \mathbf{S}^e \mathbf{U}^e \mathbf{R}^{e\top} = J^{-1} \mathbf{R}^e \left(\sum_{i=1}^3 \lambda_i^e \frac{\partial \check{\psi}^{(1)}(\lambda_1^e, \lambda_2^e, \lambda_3^e, \vartheta)}{\partial \lambda_i^e} \mathbf{r}_i^e \otimes \mathbf{r}_i^e \right) \mathbf{R}^{e\top}. \quad (4.6)$$

Next, since $\mathbf{M}^e = \mathbf{C}^e \mathbf{S}^e$ (cf. (3.5)), use of (4.1) and (4.5) gives the Mandel stress as

$$\mathbf{M}^e = \sum_{i=1}^3 \lambda_i^e \frac{\partial \check{\psi}^{(1)}(\lambda_1^e, \lambda_2^e, \lambda_3^e, \vartheta)}{\partial \lambda_i^e} \mathbf{r}_i^e \otimes \mathbf{r}_i^e. \quad (4.7)$$

Let

$$\mathbf{E}^e \stackrel{\text{def}}{=} \ln \mathbf{U}^e = \sum_{i=1}^3 E_i^e \mathbf{r}_i^e \otimes \mathbf{r}_i^e, \quad (4.8)$$

denote the logarithmic elastic strain with principal values

$$E_i^e \stackrel{\text{def}}{=} \ln \lambda_i^e, \quad (4.9)$$

and consider an elastic free energy function of the form

$$\check{\psi}^{(1)}(\lambda_1^e, \lambda_2^e, \lambda_3^e, \vartheta) = \check{\psi}^{(1)}(E_1^e, E_2^e, E_3^e, \vartheta), \quad (4.10)$$

so that, using (4.7),

$$\mathbf{M}^e = \sum_{i=1}^3 \frac{\partial \check{\psi}^{(1)}(E_1^e, E_2^e, E_3^e, \vartheta)}{\partial E_i^e} \mathbf{r}_i^e \otimes \mathbf{r}_i^e. \quad (4.11)$$

We consider the following simple generalization of the classical strain energy function of infinitesimal isotropic elasticity which uses a logarithmic measure of finite strain⁶

$$\check{\psi}^{(1)}(\mathbf{E}^e, \vartheta) = G |\mathbf{E}^e|^2 + \frac{1}{2} (K - \frac{2}{3} G) (\text{tr } \mathbf{E}^e)^2 - (\vartheta - \vartheta_0) (3 K \alpha) (\text{tr } \mathbf{E}^e) + \tilde{f}(\vartheta), \quad (4.12)$$

⁶This is a useful free energy function for *moderately large elastic stretches*, Anand (1979, 1986).

where $\tilde{f}(\vartheta)$ is an entropic contribution to the free energy related to the temperature-dependent specific heat of the material. The temperature-dependent parameters

$$G(\vartheta) > 0, \quad K(\vartheta) > 0, \quad \alpha(\vartheta) > 0, \quad (4.13)$$

are the shear modulus, bulk modulus, and coefficient of thermal expansion, respectively, and ϑ_0 is a reference temperature. Then, (4.11) gives

$$\mathbf{M}^e = 2G\mathbf{E}_0^e + K(\text{tr}\mathbf{E}^e)\mathbf{1} - 3K\alpha(\vartheta - \vartheta_0)\mathbf{1}, \quad (4.14)$$

and on account of (4.6), (4.7), and (4.14),

$$\mathbf{T}^{(1)} = J^{-1}\mathbf{R}^e\mathbf{M}^e\mathbf{R}^{e\top}. \quad (4.15)$$

4.2 Free energy $\psi^{(2)}$

We denote the distortional part of \mathbf{F} by⁷

$$\mathbf{F}_{\text{dis}} \stackrel{\text{def}}{=} J^{-1/3}\mathbf{F}, \quad \det\mathbf{F}_{\text{dis}} = 1. \quad (4.16)$$

Correspondingly, let

$$\mathbf{C}_{\text{dis}} \stackrel{\text{def}}{=} (\mathbf{F}_{\text{dis}})^\top\mathbf{F}_{\text{dis}} = J^{-2/3}\mathbf{C}, \quad (4.17)$$

denote the distortional (or volume preserving) right Cauchy-Green tensor, and consider a free energy function in the special form

$$\psi^{(2)} = \bar{\psi}^{(2)}(\mathcal{I}_{\mathbf{C}_{\text{dis}}}, \vartheta), \quad (4.18)$$

where $\mathcal{I}_{\mathbf{C}_{\text{dis}}}$ are the principal invariants of \mathbf{C}_{dis} . Then using (3.4)₂ the stress \mathbf{S} with a free energy of the form above is

$$\mathbf{S} = 2\frac{\partial\bar{\psi}^{(2)}(\mathcal{I}_{\mathbf{C}_{\text{dis}}}, \vartheta)}{\partial\mathbf{C}} = 2\left\{\frac{\partial\mathbf{C}_{\text{dis}}}{\partial\mathbf{C}}\right\}^\top\frac{\partial\bar{\psi}^{(2)}(\mathcal{I}_{\mathbf{C}_{\text{dis}}}, \vartheta)}{\partial\mathbf{C}_{\text{dis}}}. \quad (4.19)$$

Next, since $J = \sqrt{\det\mathbf{C}}$, and since

$$\frac{\partial\det\mathbf{C}}{\partial\mathbf{C}} = (\det\mathbf{C})\mathbf{C}^{-1} = J^2\mathbf{C}^{-1},$$

we have

$$\frac{\partial J}{\partial\mathbf{C}} = \frac{1}{2}J\mathbf{C}^{-1}, \quad \text{and} \quad \frac{\partial J^{-2/3}}{\partial\mathbf{C}} = -\frac{1}{3}J^{-2/3}\mathbf{C}^{-1}. \quad (4.20)$$

Also,

$$\frac{\partial\mathbf{C}_{\text{dis}}}{\partial\mathbf{C}} = \frac{\partial(J^{-2/3}\mathbf{C})}{\partial\mathbf{C}} = J^{-2/3}(\mathbb{I} + J^{-2/3}\mathbf{C} \otimes \frac{\partial J^{-2/3}}{\partial\mathbf{C}}),$$

or using (4.20)₂,

$$\frac{\partial\mathbf{C}_{\text{dis}}}{\partial\mathbf{C}} = J^{-2/3}\left(\mathbb{I} - \frac{1}{3}\mathbf{C} \otimes \mathbf{C}^{-1}\right) = J^{-2/3}\left(\mathbb{I} - \frac{1}{3}\mathbf{C}_{\text{dis}} \otimes \mathbf{C}_{\text{dis}}^{-1}\right), \quad (4.21)$$

where \mathbb{I} is the fourth-order identity tensor. Thus, using (4.20)₁ and (4.21) in (4.19), the stress \mathbf{S} has the form

$$\begin{aligned} \mathbf{S} &= 2J^{-2/3}\left(\mathbb{I} - \frac{1}{3}\mathbf{C}_{\text{dis}}^{-1} \otimes \mathbf{C}_{\text{dis}}\right)\frac{\partial\bar{\psi}^{(2)}(\mathcal{I}_{\mathbf{C}_{\text{dis}}}, \vartheta)}{\partial\mathbf{C}_{\text{dis}}} \\ &= 2J^{-2/3}\left[\frac{\partial\bar{\psi}^{(2)}(\mathcal{I}_{\mathbf{C}_{\text{dis}}}, \vartheta)}{\partial\mathbf{C}_{\text{dis}}} - \frac{1}{3}\left(\mathbf{C}_{\text{dis}} : \frac{\partial\bar{\psi}^{(2)}(\mathcal{I}_{\mathbf{C}_{\text{dis}}}, \vartheta)}{\partial\mathbf{C}_{\text{dis}}}\right)\mathbf{C}_{\text{dis}}^{-1}\right]. \end{aligned} \quad (4.22)$$

⁷Since $J^e = J$, and since we have already accounted for a volumetric elastic energy for $\psi^{(1)}$, we do not allow for a volumetric elastic energy for $\psi^{(2)}$.

In order to model the stress increase due to the stretching and locking of polymer chains at large strains, most previous theories for amorphous polymers (e.g., Parks et al., 1985; Boyce et al., 1988; Arruda and Boyce, 1993; Wu and Van der Giessen, 1993a; Anand and Gurtin, 2003) presume that polymer glasses behave like crosslinked rubber and use a free energy based on *entropic-network* models. There is a conceptual difficulty with using statistical-mechanical ideas of the theory of entropic rubber elasticity to describe the strain hardening due to chain-alignment at temperatures below the glass transition temperature, because at these temperatures the chains do not have sufficient mobility in the amorphous state to sample all possible molecular conformations, as visualized in the statistical-mechanical models of rubber elasticity (Anand and Ames, 2006). Here, we employ a simple *phenomenological* form for the free energy function $\psi^{(2)}$ due to Gent (1996).⁸ With

$$I_1 \stackrel{\text{def}}{=} \text{tr} \mathbf{C}_{\text{dis}} \quad (4.23)$$

denoting the first principal invariant of \mathbf{C}_{dis} , the Gent free energy has the form

$$\psi^{(2)} = -\frac{1}{2} \mu_{\text{R}} I_m \ln \left(1 - \frac{I_1 - 3}{I_m} \right), \quad (4.24)$$

which involves two temperature-dependent material parameters

$$\mu_{\text{R}}(\vartheta) > 0, \quad I_m(\vartheta) > 3. \quad (4.25)$$

In particular, μ_{R} represents the ground state rubbery shear modulus of the material, and I_m represents the upper limit of $(I_1 - 3)$, associated with limited chain extensibility of polymeric molecules. For this simple free energy,

$$\frac{\partial \bar{\psi}^{(2)}(\mathcal{I}_{\mathbf{C}_{\text{dis}}}, \vartheta)}{\partial \mathbf{C}_{\text{dis}}} = \frac{1}{2} \mu_{\text{R}} \left(1 - \frac{I_1 - 3}{I_m} \right)^{-1} \frac{\partial I_1}{\partial \mathbf{C}_{\text{dis}}} = \frac{1}{2} \mu_{\text{R}} \left(1 - \frac{I_1 - 3}{I_m} \right)^{-1} \mathbf{1}. \quad (4.26)$$

Using (4.26) in (4.22) gives

$$\mathbf{S} = J^{-2/3} \mu_{\text{R}} \left(1 - \frac{I_1 - 3}{I_m} \right)^{-1} \left[\mathbf{1} - \frac{1}{3} \left(\text{tr} \mathbf{C}_{\text{dis}} \right) \mathbf{C}_{\text{dis}}^{-1} \right]. \quad (4.27)$$

Next, from (3.4)₁, the contribution $\mathbf{T}^{(2)}$ to the Cauchy stress is

$$\mathbf{T}^{(2)} = J^{-1} \mathbf{F} \mathbf{S} \mathbf{F}^{\top} = J^{-1/3} \mathbf{F}_{\text{dis}} \mathbf{S} \mathbf{F}_{\text{dis}}^{\top}, \quad (4.28)$$

and hence, using (4.27),

$$\mathbf{T}^{(2)} = J^{-1} \mu_{\text{R}} \left(1 - \frac{I_1 - 3}{I_m} \right)^{-1} \left[\mathbf{F}_{\text{dis}} \mathbf{F}_{\text{dis}}^{\top} - \frac{1}{3} \left(\text{tr} \mathbf{C}_{\text{dis}} \right) \mathbf{F}_{\text{dis}} \mathbf{C}_{\text{dis}}^{-1} \mathbf{F}_{\text{dis}}^{\top} \right].$$

Then with

$$\mathbf{B}_{\text{dis}} \stackrel{\text{def}}{=} \mathbf{F}_{\text{dis}} \mathbf{F}_{\text{dis}}^{\top}, \quad (4.29)$$

$$\mathbf{T}^{(2)} = J^{-1} \mu_{\text{R}} \left(1 - \frac{I_1 - 3}{I_m} \right)^{-1} \left[\mathbf{B}_{\text{dis}} - \frac{1}{3} \left(\text{tr} \mathbf{B}_{\text{dis}} \right) \mathbf{1} \right],$$

or

$$\mathbf{T}^{(2)} = J^{-1} \mu_{\text{R}} \left(1 - \frac{I_1 - 3}{I_m} \right)^{-1} (\mathbf{B}_{\text{dis}})_0. \quad (4.30)$$

⁸This model has been shown by Boyce (1996) to yield predictions for the stress-strain response similar to the entropic-network model of Arruda and Boyce (1993).

4.3 Free energy $\psi^{(p)}$

The spectral representation of \mathbf{A} is

$$\mathbf{A} = \sum_{i=1}^3 a_i \mathbf{l}_i \otimes \mathbf{l}_i, \quad (4.31)$$

where (a_1, a_2, a_3) are the positive eigenvalues, and $(\mathbf{l}_1, \mathbf{l}_2, \mathbf{l}_3)$ are the orthonormal eigenvectors of \mathbf{A} . The principal invariants of \mathbf{A} are:

$$\left. \begin{aligned} I_1(\mathbf{A}) &= a_1 + a_2 + a_3, \\ I_2(\mathbf{A}) &= a_1 a_2 + a_2 a_3 + a_3 a_1, \\ I_3(\mathbf{A}) &= a_1 a_2 a_3 = 1 \quad (\text{since } \det \mathbf{A} = 1). \end{aligned} \right\} \quad (4.32)$$

Using (4.32), we express the defect energy as

$$\psi^{(p)} = \tilde{\psi}^{(p)}(\mathcal{I}_{\mathbf{A}}, \vartheta) = \check{\psi}^{(p)}(a_1, a_2, a_3, \vartheta). \quad (4.33)$$

Then, by the chain-rule

$$\frac{\partial \check{\psi}^{(p)}(a_1, a_2, a_3, \vartheta)}{\partial \mathbf{A}} = \sum_{i=1}^3 \frac{\partial \check{\psi}^{(p)}(a_1, a_2, a_3, \vartheta)}{\partial a_i} \frac{\partial a_i}{\partial \mathbf{A}}. \quad (4.34)$$

Assume that a_i are distinct, so that the a_i and the principal directions \mathbf{l}_i may be considered as functions of \mathbf{A} . Then,

$$\frac{\partial a_i}{\partial \mathbf{A}} = \mathbf{l}_i \otimes \mathbf{l}_i, \quad (4.35)$$

and, granted this, (4.34) implies that

$$\frac{\partial \check{\psi}^{(p)}(a_1, a_2, a_3, \vartheta)}{\partial \mathbf{A}} = \sum_{i=1}^3 \frac{\partial \check{\psi}^{(p)}(a_1, a_2, a_3, \vartheta)}{\partial a_i} \mathbf{l}_i \otimes \mathbf{l}_i. \quad (4.36)$$

Also, use of (4.31) and (4.36) in (3.6) gives the deviatoric back-stress as

$$\mathbf{M}_{\text{back}} = 2 \left(\sum_{i=1}^3 a_i \frac{\partial \check{\psi}^{(p)}(a_1, a_2, a_3, \vartheta)}{\partial a_i} \mathbf{l}_i \otimes \mathbf{l}_i \right)_0. \quad (4.37)$$

Next, we consider the following simple defect energy:

$$\check{\psi}^{(p)}(a_1, a_2, a_3, \vartheta) = \frac{1}{4} B [(\ln a_1)^2 + (\ln a_2)^2 + (\ln a_3)^2], \quad (4.38)$$

with $B(\vartheta) > 0$. Then

$$\frac{\partial \check{\psi}^{(p)}(a_1, a_2, a_3, \vartheta)}{\partial \mathbf{A}} = \frac{1}{2} B \sum_{i=1}^3 \frac{\ln a_i}{a_i} \mathbf{l}_i \otimes \mathbf{l}_i = \frac{1}{2} B (\ln \mathbf{A}) \mathbf{A}^{-1}, \quad (4.39)$$

where

$$\ln \mathbf{A} \stackrel{\text{def}}{=} \sum_{i=1}^3 \ln a_i \mathbf{l}_i \otimes \mathbf{l}_i, \quad (4.40)$$

and

$$\mathbf{A}^{-1} = \sum_{i=1}^3 a_i^{-1} \mathbf{l}_i \otimes \mathbf{l}_i. \quad (4.41)$$

Then, using (4.39) in (4.37) gives

$$\mathbf{M}_{\text{back}} = B (\ln \mathbf{A})_0. \quad (4.42)$$

Note that since $a_1 a_2 a_3 = 1$ (cf. (4.32)₃),

$$\text{tr}(\ln \mathbf{A}) = \ln a_1 + \ln a_2 + \ln a_3 = \ln(a_1 a_2 a_3) = 0.$$

Hence the defect strain tensor ($\ln \mathbf{A}$) is *traceless*, and therefore

$$\mathbf{M}_{\text{back}} = B \ln \mathbf{A}; \quad (4.43)$$

we call the positive-valued constitutive parameter $B(\vartheta) \geq 0$ the *back-stress modulus*.

4.4 Strength function. Internal variables

Here we are concerned with specializing the strength relation

$$|(\mathbf{M}_{\text{eff}}^e)_0| = Y(d^p, \mathbf{\Lambda}) \quad \text{with} \quad \mathbf{\Lambda} = \{\mathbf{C}^e, \mathbf{B}^p, \mathbf{A}, \boldsymbol{\xi}, \vartheta\}, \quad (4.44)$$

appearing in (3.12).

First, we define an *equivalent shear stress* by

$$\bar{\tau} \stackrel{\text{def}}{=} \frac{1}{\sqrt{2}} |(\mathbf{M}_{\text{eff}}^e)_0|, \quad (4.45)$$

and an *equivalent shear strain rate* by

$$\nu^p \stackrel{\text{def}}{=} \sqrt{2} d^p = \sqrt{2} |\mathbf{D}^p|, \quad (4.46)$$

respectively.

Next, recalling (4.14) for the Mandel stress \mathbf{M}^e , we define the *mean normal pressure* by

$$\bar{p} \stackrel{\text{def}}{=} -\frac{1}{3} \text{tr} \mathbf{M}^e = -K \{ \text{tr} \mathbf{E}^e - 3\alpha(\vartheta - \vartheta_0) \} = -K \left\{ \frac{1}{2} \text{tr}(\ln \mathbf{C}^e) - 3\alpha(\vartheta - \vartheta_0) \right\}. \quad (4.47)$$

Also let

$$\bar{\lambda}^p \stackrel{\text{def}}{=} \sqrt{\text{tr} \mathbf{B}^p / 3} \quad (4.48)$$

define an *effective plastic stretch*. Then, as an (enormous) simplification of the theory, we assume that the strength function Y is independent of \mathbf{A} , and depends on \mathbf{C}^e and \mathbf{B}^p only through \bar{p} and $\bar{\lambda}^p$.

Further, we restrict the list $\boldsymbol{\xi}$ of internal variables to three scalars

$$\varphi, \quad S_1, \quad \text{and} \quad S_2.$$

The two parameters φ and S_1 are introduced to model the “yield-peak” of glassy polymers. A key microstructural feature controlling the strain-softening associated with the “yield-peak” is the deformation-induced disordering of glassy polymers.⁹ The variable φ , a positive-valued dimensionless “order”-parameter, is introduced to represent such *deformation-induced disordering*; and S_1 , a stress-dimensioned internal variable, represents the corresponding *transient resistance* to plastic flow accompanying the microstructural disordering. The parameter S_2 , another positive-valued stress-dimensioned internal variable, is introduced to model additional “isotropic”-hardening aspects of the stress-strain response of these material as the chains are pulled taut between entanglements at large strains.

With these simplifications and internal variables, and using the definitions (4.45) – (4.48), we rewrite the strength relation (4.44)₁ as

$$\bar{\tau} = g(\nu^p, \vartheta, \bar{p}, \bar{\lambda}^p, \varphi, S_1, S_2), \quad (4.49)$$

⁹The deformation-induced disordering is often associated with the change in “free-volume” of glassy polymers. The “free-volume” terminology was introduced by by Cohen and Grest (1979) for simple atomic glasses (amorphous metals), and there is a corresponding way to define it in glassy polymers (Shah et al., 1989). The deformation-induced disordering and its role in the yield drop in amorphous materials has also been discussed recently by Argon and Demkowicz (2008) (in the context of amorphous silicon).

and assume further that at a fixed state $(\vartheta, \bar{p}, \bar{\lambda}^p, \varphi, S_1, S_2)$ the strength relation (4.49) is *invertible*, with inverse

$$\nu^p = f(\bar{\tau}, \vartheta, \bar{p}, \bar{\lambda}^p, \varphi, S_1, S_2) \geq 0. \quad (4.50)$$

Finally, guided by the literature (cf., e.g., Fotheringham and Cherry, 1976, 1978; Povolò and Hermida, 1995, 1996; Richeton et al., 2005, 2006, 2007), for the flow function f in (4.50) we choose a thermally-activated relation in the specific form

$$\nu^p = \begin{cases} 0 & \text{if } \tau_e \leq 0, \\ \nu_0 \exp\left\{-\frac{Q}{k_B \vartheta}\right\} \left[\sinh\left(\frac{\tau_e V}{2k_B \vartheta}\right)\right]^{1/m} & \text{if } \tau_e > 0, \end{cases} \quad (4.51)$$

where

$$\tau_e \stackrel{\text{def}}{=} \bar{\tau} - (S_1 + S_2 + \alpha_p \bar{p}) \quad (4.52)$$

denotes a *net shear stress for thermally activated flow*, and where $\alpha_p \geq 0$ is parameter introduced to account for the *pressure sensitivity* of plastic flow. Additionally, ν_0 is a pre-exponential factor with dimensions of s^{-1} , Q is an *activation energy*, k_B is Boltzmann's constant, V is an *activation volume*, and m is a *strain rate sensitivity parameter*.

Some remarks: There are many models for the rate and temperature-dependent yield strength of polymers in the literature which consider plastic flow as a thermally-activated process (cf., e.g., Eyring, 1936; Robertson, 1966; Argon, 1973). Most of these models give a reasonably acceptable representation of the variation of the yield strength with temperature and strain rate, but over limited ranges of these variables. The flow function (4.51) used here is motivated by the recent work of Richeton et al. (2005, 2006, 2007), who in turn base their model on the so-called “cooperative”-model of Fotheringham and Cherry (1976, 1978) and Povolò and Hermida (1995, 1996). Richeton et al. have shown that a flow function of the form (4.51) may be used to satisfactorily represent the variation of the yield strength of amorphous polymers over a wide range of strain rates and temperatures.¹⁰ The major difference between the flow function proposed by Richeton et al. and the one considered here, is that instead of a tensorial back-stress \mathbf{M}_{back} (cf., (4.43)) to define an effective stress which drives plastic flow (cf. (3.8)), they consider a temperature dependent scalar internal stress in their theory. This results in a profound difference between their model and the one considered here, specially in the ability of the two models to capture unloading and cyclic loading phenomena, as well as in a proper accounting of the energy dissipated during plastic flow. Also, the three-dimensional theory that they present in §3 of their 2007 paper is substantially different in its mathematical structure from that considered here.

Mulliken and Boyce (2006), have recently proposed an alternate model to describe the variation of the yield strength of amorphous polymers over a wide range of strain rates and temperatures, albeit still for temperatures below the glass transition. Their model is a generalization of the model(s) proposed by Bauwens, Bauwens-Crowet et al., and co-workers (cf., e.g., Bauwens et al. 1969; Bauwens, 1972; Bauwens-Crowet et al., 1969, 1972; Bauwens-Crowet, 1973), in which they introduce two rheological micro-mechanisms – designated as primary or α and secondary or β – which contribute to the yield strength of the material. The primary α -mechanism represents the rotations of the main-chain segments of the polymer, and the secondary β -mechanism represents the rotations of the ester side groups in PMMA, and the rotations of the phenyl groups in the main chains of PC. These two mechanisms are rate-limiting in different regimes of strain rates and/or temperatures; the α -mechanism is the dominant rate-limiting mechanism at low rates (or high temperatures), and the β -mechanism is the dominant rate-limiting mechanism at high strain rates (or low temperatures). Mulliken and Boyce assume that the α and β molecular processes are sufficiently decoupled, so that the overall material response may be described by a simple superposition of the two mechanisms. Accordingly, in the three-dimensional version of their theory, instead of using the standard Kröner (1960) decomposition $\mathbf{F} = \mathbf{F}^e \mathbf{F}^p$ as done here, they develop a theory which employs a decomposition of the form $\mathbf{F} = \mathbf{F}_\alpha^e \mathbf{F}_\alpha^p = \mathbf{F}_\beta^e \mathbf{F}_\beta^p$ to account for the α and β mechanisms. This results in a substantially different and more complex constitutive theory than that considered here, and also results in a doubling of the material

¹⁰Richeton et al. extend the flow rule (4.51) through the glass transition temperature, but in this paper we fix our attention in the regime of temperatures below ϑ_g .

parameters concerning pre-exponential factors, activation energies, deformation resistances, press-sensitivity parameters, and so on.

Whatever the physical merits of the multi-mechanism (α, β) -based model of Mulliken and Boyce, for operational economy our preference here is not to follow their approach, but instead to adopt a variant of the “cooperative”-model of Richeton et al. (2007), which from a macroscopic point of view appears to achieve the same goal of being able to represent the variation of the yield strength of amorphous polymers over a wide range of strain rates and temperatures.

4.5 Evolution equations for the internal variables

4.5.1 Evolution of φ and S_1

We assume that the material disorders, and is accompanied by a microscale dilatation as plastic deformation occurs, resulting in an increase of the order-parameter φ ,¹¹ and this increase in disorder leads to a change in the resistance S_1 , causing a transient change in the flow stress of the material as plastic deformation proceeds. Accordingly, the evolution of the resistance S_1 is coupled to the evolution of the order-parameter φ . Specifically, we take the evolution of S_1 to be governed by¹²

$$\left. \begin{aligned} \dot{S}_1 &= H_1 \nu^p, & \text{with initial value } S_1(\mathbf{X}, 0) &= S_{1i}, \\ H_1 &= h_1 (S_1^* - S_1), & \text{and } S_1^* &= \hat{S}_1^*(\nu^p, \vartheta, \varphi), \end{aligned} \right\} \quad (4.53)$$

and we assume that

$$\left. \begin{aligned} \dot{\varphi} &= \beta \nu^p & \text{with initial value } \varphi(\mathbf{X}, 0) &= \varphi_i, \\ \beta &= g (\varphi^* - \varphi), & \text{with } \varphi^* &= \hat{\varphi}^*(\nu^p, \vartheta) \geq 0; \end{aligned} \right\} \quad (4.54)$$

here β is a *shear-induced disordering function*.¹³

In these coupled evolution equations for S_1 and φ , the parameters h_1 , g , S_{1i} and φ_i are constants (possibly temperature-dependent). The function H_1 represents the strain-hardening/softening function for the resistance S_1 during plastic flow: the material hardens ($H_1 > 0$) if $S_1 < S_1^*$, and softens ($H_1 < 0$) if $S_1 > S_1^*$. The critical value S_1^* of S_1 controlling such hardening/softening transitions is assumed to depend on the current values of the plastic strain rate, temperature, and the order-parameter φ . In the disordering function β , the parameter φ^* represents a strain rate and temperature dependent critical value for the order-parameter: the material disorders ($\beta > 0$) when $\varphi < \varphi^*$, and becomes less disordered ($\beta < 0$) when $\varphi > \varphi^*$. In a monotonic experiment at a given strain rate and temperature, the shear-induced disordering vanishes ($\beta = 0$) when $\varphi = \varphi^*$. However, in an experiment in which the strain rate and temperature are varying (e.g. strain rate or temperature jump experiments), the material will in general increase or decrease in disorder, depending on the strain rate and temperature history, and because of the coupling between the evolution equations for S_1 and φ , the resistance S_1 will also vary.

Particular forms for the function $\hat{\varphi}^*(\nu^p, \vartheta)$ and $\hat{S}_1^*(\nu^p, \vartheta, \varphi)$ need to be specified. The function φ^* controls the amount of disordering the material undergoes during deformation and is both strain rate and temperature dependent. The strain rate and temperature dependence of φ^* is quite nonlinear; φ^* is expected to decrease with increasing temperature at a fixed strain rate, and increase with strain rate at a fixed temperature. We model this temperature and strain rate dependence of φ^* using the following phenomenological form

$$\hat{\varphi}^*(\nu^p, \vartheta) = \begin{cases} \varphi_r \left[1 + \left(\frac{\vartheta_c - \vartheta}{k} \right)^r \right] \left(\frac{\nu^p}{\nu_r} \right)^s & \text{for } \vartheta < \vartheta_c, \\ 0 & \text{for } \vartheta > \vartheta_c, \end{cases} \quad (4.55)$$

¹¹The microscale dilatation is extremely small, and at the macroscopic level we presume the plastic flow to be incompressible.

¹²Coupled differential evolution equations of this type have previously been used to model yield peaks in granular materials (Anand and Gu, 2000), as well as amorphous polymeric materials (Anand and Gurtin, 2003) and amorphous metallic glasses (Henann and Anand, 2008).

¹³We concentrate only on deformation-induced disordering, and neglect any decrease in the degree of disorder due to temperature-dependent recovery effects in the absence of macroscopic plastic deformation.

where ϑ_c is as strain rate dependent function given by¹⁴

$$\vartheta_c = \begin{cases} \vartheta_g + n \ln \left(\frac{\nu^p}{\nu_r} \right) & \text{for } \nu^p > \nu_r, \\ \vartheta_g & \text{for } \nu^p \leq \nu_r, \end{cases} \quad (4.56)$$

with $\{\varphi_r, k, r, s, \nu_r, n\}$ as constants.

Further, the function S_1^* , which controls the magnitude of the stress-overshoot, is taken as

$$S_1^* = b(\varphi^* - \varphi), \quad (4.57)$$

so that the value of S_1^* depends linearly on the difference between the current value of φ and the parameter φ^* .

Thus, gathering the number of material parameters introduced to phenomenologically model the yield-peak, we have the following rather large list

$$\{h_1, b, S_{1i}, g, \varphi_i, \varphi_r, k, r, s, \nu_r, n\},$$

with some of these parameters possessing additional temperature-dependence. *We note that modeling the temperature and rate-sensitivity of the yield-peak over a wide-range of temperatures and strain rates is notoriously difficult.* If a simpler theory with fewer material parameters is desired, and if it is deemed that modeling the yield-peak is not of interest, then there is no need to introduce the internal variables φ and S_1 , and thereby also the attendant constants in their evolution equations.

4.5.2 Evolution of S_2

The evolution of S_2 is taken to be governed by

$$\dot{S}_2 = h_2 (\bar{\lambda}^p - 1) (S_2^* - S_2) \nu^p \quad \text{with initial value } S_2(\mathbf{X}, 0) = S_{2i} \geq 0, \quad (4.58)$$

where h_2 is assumed to be constant and $S_2^*(\vartheta)$ is a temperature dependent material parameter. The resistance S_2 increases and the material hardens as long as $S_2 < S_2^*$.

4.5.3 Evolution of \mathbf{A}

Finally, the evolution equation for \mathbf{A} is taken as

$$\dot{\mathbf{A}} = \mathbf{D}^p \mathbf{A} + \mathbf{A} \mathbf{D}^p - \gamma \mathbf{A} \ln \mathbf{A} \nu^p, \quad \mathbf{A}(\mathbf{X}, 0) = \mathbf{1}, \quad (4.59)$$

where $\gamma \geq 0$ is a constitutive parameter which governs the dynamic recovery of \mathbf{A} . This evolution equation is a generalization of the non-linear kinematic-hardening rule (Armstrong and Fredrick, 1966) of the small deformation theory of classical metal viscoplasticity,¹⁵ but here applied to polymer-viscoplasticity.

4.6 Summary of the specialized constitutive model. Partial differential equations for the deformation and temperature fields

In this section, we summarize the specialized form of our theory, which should be useful in applications. We also list the partial differential equations for the deformation and temperature fields.

¹⁴This approximately models the rate-dependence of the glass transition temperature of the material.

¹⁵Cf., e.g., Chaboche (2008) for a recent review of the large variety of kinematic-hardening rules in classical small deformation metal-viscoplasticity.

4.6.1 Constitutive equations

1. Free energy

We consider a separable free energy

$$\psi_{\text{R}} = \psi^{(1)} + \psi^{(2)} + \psi^{(p)}. \quad (4.60)$$

With

$$\mathbf{U}^e = \sum_{i=1}^3 \lambda_i^e \mathbf{r}_i^e \otimes \mathbf{r}_i^e, \quad (4.61)$$

denoting the spectral representation of \mathbf{U}^e , and with

$$\mathbf{E}^e = \sum_{i=1}^3 E_i^e \mathbf{r}_i^e \otimes \mathbf{r}_i^e, \quad E_i^e = \ln \lambda_i^e, \quad (4.62)$$

denoting an elastic logarithmic strain measure, we adopt the following special form for the free energy $\psi^{(1)}$:

$$\psi^{(1)} = G|\mathbf{E}^e|^2 + \frac{1}{2}(K - \frac{2}{3}G)(\text{tr } \mathbf{E}^e)^2 - (\vartheta - \vartheta_0)(3K\alpha)(\text{tr } \mathbf{E}^e) + \tilde{f}(\vartheta), \quad (4.63)$$

where $\tilde{f}(\vartheta)$ is an entropic contribution to the free energy related to the temperature-dependent specific heat of the material. The temperature-dependent parameters

$$G(\vartheta) > 0, \quad K(\vartheta) > 0, \quad \alpha(\vartheta) > 0, \quad (4.64)$$

are the shear modulus, bulk modulus, and coefficient of thermal expansion, respectively, and ϑ_0 is a reference temperature.

Next, with

$$I_1 \stackrel{\text{def}}{=} \text{tr } \mathbf{C}_{\text{dis}} \quad (4.65)$$

denoting the first principal invariant of \mathbf{C}_{dis} . We adopt the following special form for free energy $\psi^{(2)}$

$$\psi^{(2)} = -\frac{1}{2}\mu_{\text{R}} I_m \ln \left(1 - \frac{I_1 - 3}{I_m} \right), \quad (4.66)$$

where

$$\mu_{\text{R}}(\vartheta) > 0, \quad I_m(\vartheta) > 3 \quad (4.67)$$

are two temperature-dependent material constants. In particular, μ_{R} represents the ground state rubbery shear modulus of the material, and I_m represents the upper limit of $(I_1 - 3)$, associated with limited chain extensibility.

Further, with

$$\mathbf{A} = \sum_{i=1}^3 a_i \mathbf{l}_i \otimes \mathbf{l}_i, \quad (4.68)$$

denoting the spectral representation of \mathbf{A} , and with

$$\ln \mathbf{A} = \sum_{i=1}^3 \ln a_i \mathbf{l}_i \otimes \mathbf{l}_i, \quad (4.69)$$

denoting a defect logarithmic strain measure, we adopt a free energy $\psi^{(p)}$ of the form

$$\psi^{(p)} = \frac{1}{4}B [(\ln a_1)^2 + (\ln a_2)^2 + (\ln a_3)^2], \quad (4.70)$$

where the positive-valued temperature-dependent parameter

$$B(\vartheta) \geq 0, \quad (4.71)$$

is a back-stress modulus.

2. Cauchy stress. Mandel stress. Back-stress. Effective stress

Corresponding to the special free energy functions considered above, the Cauchy stress is given by

$$\mathbf{T} = \mathbf{T}^{(1)} + \mathbf{T}^{(2)}, \quad (4.72)$$

with

$$\mathbf{T}^{(1)} = J^{-1} \mathbf{R}^e \mathbf{M}^e \mathbf{R}^{e\tau}, \quad (4.73)$$

where

$$\mathbf{M}^e = 2G\mathbf{E}_0^e + K(\text{tr}\mathbf{E}^e)\mathbf{1} - 3K\alpha(\vartheta - \vartheta_0)\mathbf{1}, \quad (4.74)$$

is the Mandel stress, and

$$\mathbf{T}^{(2)} = J^{-1} \mu_R \left(1 - \frac{I_1 - 3}{I_m}\right)^{-1} (\mathbf{B}_{\text{dis}})_0. \quad (4.75)$$

The symmetric and deviatoric back-stress is defined by

$$\mathbf{M}_{\text{back}} = B \ln \mathbf{A}, \quad (4.76)$$

and the driving stress for plastic flow is the effective stress given by

$$(\mathbf{M}_{\text{eff}}^e)_0 = \mathbf{M}_0^e - \mathbf{M}_{\text{back}}. \quad (4.77)$$

The corresponding *equivalent shear stress* and *mean normal pressure* are given by

$$\bar{\tau} \stackrel{\text{def}}{=} \frac{1}{\sqrt{2}} |(\mathbf{M}_{\text{eff}}^e)_0|, \quad \text{and} \quad \bar{p} \stackrel{\text{def}}{=} -\frac{1}{3} \text{tr} \mathbf{M}^e, \quad (4.78)$$

respectively.

3. Internal variables

The internal variables of the theory

$$\varphi \geq 0, \quad S_1 \geq 0, \quad S_2 \geq 0,$$

represent aspects of the intermolecular shear resistance to plastic flow. The parameter φ is a dimensionless order-parameter representing a local measure of disorder of the polymeric glass; S_1 and S_2 have dimensions of stress and, respectively, represent aspects of a transient shear resistance accompanying microstructural disordering, and aspects of increased shear resistance to plastic flow as the chains are pulled taut between entanglements at large strains.

4. Flow rule

The evolution equation for \mathbf{F}^p is

$$\left. \begin{aligned} \dot{\mathbf{F}}^p &= \mathbf{D}^p \mathbf{F}^p, & \mathbf{F}^p(\mathbf{X}, 0) &= \mathbf{1}, \\ \mathbf{D}^p &= \nu^p \left(\frac{(\mathbf{M}_{\text{eff}}^e)_0}{2\bar{\tau}} \right), \\ \tau_e &= \bar{\tau} - (S_1 + S_2 + \alpha_p \bar{p}), \\ \nu^p &= \begin{cases} 0 & \text{if } \tau_e \leq 0, \\ \nu_0 \exp \left\{ -\frac{Q}{k_B \vartheta} \right\} \left[\sinh \left(\frac{\tau_e V}{2k_B \vartheta} \right) \right]^{1/m} & \text{if } \tau_e > 0, \end{cases} \end{aligned} \right\} \quad (4.79)$$

where τ_e denotes a *net shear stress for thermally-activated flow*; α_p is a pressure-sensitivity parameter; ν_0 is a *pre-exponential factor* with units of 1/time; Q is an *activation energy*; k_B is Boltzmann's constant; V is an *activation volume*; and m is a *strain rate sensitivity parameter*.

5. Evolution equations for the internal variables S_1 , φ , S_2 , and \mathbf{A}

The internal variables S_1 and φ are taken to obey the coupled evolution equations:

$$\dot{S}_1 = h_1 (S_1^* - S_1) \nu^p, \quad \text{with} \quad S_1^* = b(\varphi^* - \varphi), \quad \text{and} \quad S_1(\mathbf{X}, 0) = S_{1i}; \quad (4.80)$$

and

$$\text{and} \quad \left. \begin{aligned} \dot{\varphi} &= g(\varphi^* - \varphi) \nu^p, \quad \text{with} \quad \varphi(\mathbf{X}, 0) = \varphi_i, \\ \varphi^*(\nu^p, \vartheta) &= \begin{cases} \varphi_r \left[1 + \left(\frac{\vartheta_c - \vartheta}{k} \right)^r \right] \left(\frac{\nu^p}{\nu_r} \right)^s & \text{for } \vartheta \leq \vartheta_c, \\ 0 & \text{for } \vartheta > \vartheta_c, \end{cases} \\ \text{where} \quad \vartheta_c &= \begin{cases} \vartheta_g + n \ln \left(\frac{\nu^p}{\nu_r} \right) & \text{for } \nu^p > \nu_r, \\ \vartheta_g & \text{for } \nu^p \leq \nu_r, \end{cases} \end{aligned} \right\} \quad (4.81)$$

with $\{h_1, b, S_{1i}, g, \varphi_i, \varphi_r, k, r, s, \nu_r, n\}$ as material parameters.

The evolution of S_2 is taken to be governed by

$$\dot{S}_2 = h_2 (\bar{\lambda}^p - 1) (S_2^* - S_2) \nu^p, \quad \text{with} \quad S_2(\mathbf{X}, 0) = S_{2i} \geq 0, \quad (4.82)$$

where h_2 and S_2^* are constants.

Also, the evolution equation for \mathbf{A} is taken as

$$\dot{\mathbf{A}} = \mathbf{D}^p \mathbf{A} + \mathbf{A} \mathbf{D}^p - \gamma \mathbf{A} \ln \mathbf{A} \nu^p, \quad \text{with} \quad \mathbf{A}(\mathbf{X}, 0) = \mathbf{1}, \quad (4.83)$$

where $\gamma \geq 0$ is a constitutive parameter which governs the dynamic recovery of \mathbf{A} .

6. Fourier's Law:

The heat flux is taken to be governed by Fourier's law

$$\mathbf{q}_R = -\kappa \nabla \vartheta, \quad (4.84)$$

where $\kappa(\vartheta) > 0$ is the thermal conductivity.

4.6.2 Partial differential equations for the deformation and temperature fields

The partial differential equation for the deformation is obtained from the local force balance

$$\text{Div} \mathbf{T}_R + \mathbf{b}_{0R} = \rho_R \ddot{\chi}. \quad (4.85)$$

Also, balance of energy (3.17), when specialized, gives the following partial differential equation for the temperature,

$$\begin{aligned} c\dot{\vartheta} &= -\text{Div} \mathbf{q}_R + q_R + \underbrace{\left[\bar{\tau} + \frac{1}{2} B \gamma |\ln \mathbf{A}|^2 \right]}_{\text{rate of plastic dissipation}} \nu^p \\ &+ \underbrace{\frac{1}{2} \vartheta \left(\mathbf{C}^{e-1} \frac{\partial \mathbf{M}^e}{\partial \vartheta} \right) : \dot{\mathbf{C}}^e + \frac{1}{2} \vartheta \left(\frac{\partial \mathbf{S}}{\partial \vartheta} \right) : \dot{\mathbf{C}} + \frac{1}{2} \frac{\partial B(\vartheta)}{\partial \vartheta} \left((\ln \mathbf{A}) \mathbf{A}^{-1} \right) : \dot{\mathbf{A}}}_{\text{"thermoelastic-coupling" terms}}, \end{aligned} \quad (4.86)$$

where

$$\left. \begin{aligned} \frac{\partial \mathbf{M}^e}{\partial \vartheta} &= 2 \frac{\partial G(\vartheta)}{\partial \vartheta} \mathbf{E}_0^e + \frac{\partial K(\vartheta)}{\partial \vartheta} (\text{tr} \mathbf{E}^e) \mathbf{1} - 3 \frac{\partial}{\partial \vartheta} \left(K(\vartheta) \alpha(\vartheta) (\vartheta - \vartheta_0) \right) \mathbf{1}, \\ \frac{\partial \mathbf{S}}{\partial \vartheta} &= \frac{\partial}{\partial \vartheta} \left(\mu_R(\vartheta) \left(1 - \frac{I_1 - 3}{I_m(\vartheta)} \right)^{-1} \right) \mathbf{F}^{-1} (\mathbf{B}_{\text{dis}})_0 \mathbf{F}^{-\top}, \end{aligned} \right\} \quad (4.87)$$

and the specific heat in the theory is given by

$$c = \hat{c}(\mathcal{I}_{\mathbf{C}^e}, \mathcal{I}_{\mathbf{C}}, \mathcal{I}_{\mathbf{A}}, \vartheta) = -\vartheta \left[\frac{\partial^2 \bar{\psi}^{(1)}(\mathcal{I}_{\mathbf{C}^e}, \vartheta)}{\partial \vartheta^2} + \frac{\partial^2 \bar{\psi}^{(2)}(\mathcal{I}_{\mathbf{C}}, \vartheta)}{\partial \vartheta^2} + \frac{\partial^2 \bar{\psi}^p(\mathcal{I}_{\mathbf{A}}, \vartheta)}{\partial \vartheta^2} \right]. \quad (4.88)$$

At this stage of the development of the theory and the concomitant experimental database, the ‘‘thermoelastic-coupling’’ terms in (4.86) which give rise to a temperature change due to variations of \mathbf{C}^e , \mathbf{C} and \mathbf{A} are not well-characterized, nor is the dependence of the specific heat c on these quantities. *Much work needs to be done to characterize these dependencies.* Here, as *approximations*, (i) we assume that $c \approx \hat{c}(\vartheta)$ (independent of \mathbf{C}^e , \mathbf{C} and \mathbf{A}), and may be obtained from experimental measurements; and (ii) we neglect the thermoelastic coupling terms, and assume instead that only a fraction $0 \lesssim \omega \lesssim 1$ of the rate of plastic dissipation contributes to the temperature changes. Under these approximative assumptions (4.86) reduces to

$$c\dot{\vartheta} = -\text{Div} \mathbf{q}_R + q_R + \omega \left(\bar{\tau} + \frac{1}{2} B \gamma |\ln \mathbf{A}|^2 \right) \nu^p, \quad \text{with} \quad c = \hat{c}(\vartheta). \quad (4.89)$$

4.7 Temperature dependence of material parameters

Temperature dependence of the thermo-elastic moduli G , K , and α :

For polymeric materials the magnitude of the elastic shear modulus G decreases as the temperature increases, and then decreases drastically as the temperature increases through the glass transition temperature ϑ_g of the material. For temperatures below ϑ_g we approximate the change of G with temperature by

$$G(\vartheta) = G_0 - M(\vartheta - \vartheta_g) \quad \text{for} \quad \vartheta < \vartheta_g, \quad (4.90)$$

where G_0 and M are constants, and ϑ_g is the glass transition temperature.

Below the glass transition temperature, the Poisson’s ratio of the material is approximated as a constant

$$\nu_{\text{poi}} \approx \text{constant},$$

and the temperature dependence of the bulk modulus K is then obtained by using the standard relation

$$K(\vartheta) = G(\vartheta) \times \frac{2(1 + \nu_{\text{poi}})}{3(1 - 2\nu_{\text{poi}})}. \quad (4.91)$$

In the temperature range of interest, the coefficient of thermal expansion is also approximated to be constant

$$\alpha \approx \text{constant}.$$

Temperature dependence of the back-stress modulus B :

The back-stress modulus B is assumed to decrease linearly with temperature,

$$B(\vartheta) = X(\vartheta_g - \vartheta) \quad \text{for} \quad \vartheta < \vartheta_g, \quad (4.92)$$

where $X > 0$ is a constant.

Temperature dependence of the plastic flow parameters Q , V and m :

For temperatures below ϑ_g , the activation energy Q , the activation volume V , and the strain rate sensitivity parameter m appearing in the thermally activated model (4.51) are assumed to be constants.

Temperature dependence of the material parameters in the evolution equations for φ , S_1 , S_2 , and \mathbf{A}

In the coupled evolution equations (4.53) and (4.54) for S_1 and φ , the material parameters are

$$\{h_1, b, S_{1i}, g, \varphi_i, \varphi_r, k, r, s, \nu_r, n\}.$$

We assume that all but g are independent of temperature. The parameter g in (4.54) controls the width of the yield-peak where a higher values of g results in a narrower peak; this parameter is assumed to increase linearly with temperature

$$g(\vartheta) = g_1 + g_2 \vartheta \quad \text{for } \vartheta < \vartheta_g. \quad (4.93)$$

In the evolution equation (4.58) the material parameters are h_2 and S_2^* . We take h_2 to be a temperature independent constant, while the saturation value S_2^* is taken to decrease linearly with temperature, with S_2^* vanishing above ϑ_g :

$$S_2^*(\vartheta) = l_1 - l_2 \vartheta \quad \text{for } \vartheta < \vartheta_g, \quad (4.94)$$

with l_1 and l_2 constant.

In the evolution equation (4.83), the only material parameter is γ ; we take this to be temperature independent.

Temperature dependence of μ_R and I_m :

For the two material parameters μ_R and I_m in (4.25), experimental results indicate that the rubbery shear modulus μ_R decreases with increasing temperature, and the parameter I_m , which is related to limited chain extensibility, is approximately constant. The empirical function chosen to fit the experimentally-observed temperature dependence of μ_R is

$$\mu_R(\vartheta) = \mu_0 - N(\vartheta - \vartheta_g) \quad \text{for } \vartheta < \vartheta_g, \quad (4.95)$$

where μ_0 and N are constants.

Temperature dependence of specific heat c and thermal conductivity κ :

For temperatures below ϑ_g , the specific heat c and the thermal conductivity κ are assumed to have the following empirical temperature dependencies (cf., e.g. Van Krevelen, 1990; Bicerano, 1993):

$$c(\vartheta) = c_0 - c_1(\vartheta - \vartheta_g) \quad \text{for } \vartheta < \vartheta_g, \quad (4.96)$$

$$\kappa(\vartheta) = \kappa_0 \left(\frac{\vartheta}{\vartheta_g} \right)^{\kappa_1} \quad \text{for } \vartheta < \vartheta_g. \quad (4.97)$$

5 Material parameters for PMMA, PC, and Zeonex

We have implemented our thermo-mechanically-coupled constitutive model by writing a user material subroutine for the finite element program ABAQUS/Explicit (2007).

The material parameters appearing in our model were calibrated by fitting the experimental stress-strain data for PMMA, PC and Zeonex with the help of a MATLAB implementation of a one-dimensional version of our model which is detailed in the Appendix §8, as well as three-dimensional finite element simulations using a single element. Under certain circumstances, when it became necessary to account for heat generation and thermal conduction in the simple compression experiments,¹⁶ fully thermo-mechanically-coupled multi-element simulations were required. Our heuristic material parameter calibration procedure for our model is described in the Appendix. The material parameters for PMMA, PC and Zeonex determined by using this procedure are listed in Table 1.

The graphical fit of the constitutive model to the experimental stress-strain curves for PMMA at various temperatures ranging from 25 C to 100 C and strain rates ranging from 3×10^{-4} to 10^{-1} s^{-1} is shown in Fig. 3.

The fit of the constitutive model to our experimental stress-strain curves for PC at various temperatures ranging from 25 C to 130 C and strain rates ranging from 10^{-3} to 10^{-1} s^{-1} is shown in Fig. 4. The fit of the model to the high strain rate experimental stress-strain data from Garg et al. (2008) for PC at rates of 0.5 s^{-1} and 3400 s^{-1} , at an initial temperature of 25 C, is shown in Fig. 5a.¹⁷ The corresponding rise in the surface temperature of the compression specimens, as measured by Garg et al., and that predicted by the model are shown in Fig. 5b.

¹⁶Typically to fit the experimental data at a strain rate of 0.01 s^{-1} .

¹⁷Also see Bjerke et al. (2002) who report on temperature rise measurements in high rate experiments on PC.

Finally, Fig. 6 shows the fit of the constitutive model to the experimental stress-strain curves for Zeonex at various temperatures ranging from 25 C to 130 C and strain rates ranging from 3×10^{-4} to $3 \times 10^{-1} \text{ s}^{-1}$.

For all three amorphous polymers (PMMA, PC and Zeonex) studied in this paper, our continuum-mechanical, thermodynamically-consistent, large deformation constitutive model performs acceptably in reproducing the following major features of the macroscopic stress-strain response of these materials: (a) the strain rate and temperature dependent yield strength; (b) the transient yield-peak and strain-softening which occurs due to deformation-induced disordering; (c) the subsequent rapid strain-hardening due to alignment of the polymer chains at large strains; (d) the unloading response at large strains; and (e) the temperature rise due to plastic-dissipation and the limited time for heat-conduction for the compression experiments performed at strain rates $\gtrsim 0.01 \text{ s}^{-1}$. Of particular note is the feature of the constitutive model to acceptably capture the deformation response of PC over a large range of strain rates: from 10^{-3} to $3.4 \times 10^3 \text{ s}^{-1}$.¹⁸

6 Validation experiments and simulations

In order to validate the predictive capabilities of our constitutive theory and its numerical implementation, in this section we show results of some non-homogeneous experiments (which were not used to determine the material parameters in our theory), and compare the results of some key macroscopic features of the experimental results against those from the corresponding numerical simulations. Our validation experiments have been performed on either PC or Zeonex. The particular validation experiments considered below are: (i) isothermal fixed-end large-strain reversed-torsion on PC; (ii) macro-scale isothermal plane-strain cold- and hot-forming operations on PC; (iii) macro-scale isothermal, axisymmetric hot-forming operations on Zeonex; (iv) a micro-scale hot-embossing of Zeonex; and (v) high-speed normal-impact of a circular plate of PC with a spherical-tipped cylindrical projectile.

6.1 Fixed-end large-strain reversed-torsion

The torsion of a solid circular bar is a seemingly simple deformation mode. However, when the large-strain torsion is conducted with axially traction-free ends, a measurable axial extension also develops; this fascinating and complex nonlinear phenomenon is known as the *Swift-effect*.¹⁹ A complementary phenomenon is the development of an axial force when the ends of the bar are axially fixed during the large-strain torsion.

Free- or fixed-end large-strain torsion experiments provided simple yet effective means for assessing the validity of large-strain constitutive models for elastic-plastic materials.²⁰ Large-strain inelastic torsion of amorphous polymeric materials has been previously numerically studied by Wu and Van der Giessen (1993b). Here, for purposes of validating our constitutive theory, we study *fixed-end large-strain reversed torsion of a solid cylindrical specimen*. The torsion experiment was conducted at room temperature on a PC specimen with geometry shown in Fig. 7a. In the gage section, a torsion specimen has a diameter $D_0 = 31.75 \text{ mm}$, and a gage length of $L_0 = 8.89 \text{ mm}$. With ϕ denoting the angle of twist in radians, the shear-strain at the outer surface of the gage section of such a specimen is

$$\Gamma = \frac{\phi D_0}{2 L_0}. \quad (6.1)$$

The reversed-cycle torsion experiment was performed on an Instron tension-torsion servohydraulic machine, equipped with precision-aligned hydraulic grips. The machine was programmed to fix the axial displacement, and twist the specimen by rotating the grips relative to each other at an angular velocity of $\pm 0.25 \text{ deg/sec}$, which corresponds to surface shear strain rate of $\dot{\Gamma} = \pm 7.8 \times 10^{-3} \text{ s}^{-1}$ during the reversed-torsion experiment. The maximum surface shear strains achieved during the experiment, without initiating fracture, is $\Gamma \lesssim \pm 1.4$.

¹⁸High rate data for Zeonex is not currently available. Split-Hopkinson-pressure-bar high rate compression experiments for PMMA have been conducted by Mulliken and Boyce (2006), but the data is unreliable because the material crazes after relatively small strains.

¹⁹First studied by Swift (1947) for metals.

²⁰For metallic materials it has been firmly established in recent years that these axial effects in large-strain torsion arise due to the development of crystallographic texture, and that the predictions of the axial effects during torsion are strongly dependent on the constitutive model used to predict such effects (cf., e.g., Bronkhorst, Kalidindi, and Anand, 1992).

For the corresponding finite element simulation, we have modeled only the gage section and the chamfered-section of the specimen leading into the gage section. The finite element mesh, consisting of 4,801 ABAQUS-C3D8R elements, is shown in Fig 7b. The deformed geometry at a surface shear strain of $\Gamma = 1.4$ is shown in Fig 7c. Note that for the specific geometry of the torsion specimen used here, the deformation is essentially confined to the gage-section of the specimen.

Fig. 7d shows an excellent agreement between the numerically-predicted and the experimentally-measured torque versus surface shear-strain response for both forward and reversed straining. Further, Fig. 7e shows the ability of our constitutive theory to capture the major trends of the induced axial-force versus the surface shear-strain response for both forward and reversed torsional straining. Although the precise magnitudes of the axial forces are not as well-predicted as the torque response, the prediction of the actual trends for the variation of the axial forces as the shear strain is cycled, is quite remarkable.

6.2 Macro- and micro-scale, isothermal forming operations

6.2.1 Macro-scale, plane-strain, cold- and hot-forging of PC

Channel-die, plane-strain, cold- and hot-forging experiments were performed on PC specimens. The plane-strain forming operation under consideration converts a cylindrical specimen with a circular cross-section into a specimen with a cross-section which is in the shape of a “cruciform”. A schematic of a forging experiment is shown in Fig. 8. The PC specimens had an original diameter of 12.7 mm, and were 12.7 mm deep in the plane-strain direction, which is into the plane of the paper. The split-dies which impart the cruciform shape to the workpiece were made from hardened tool steel, and the interfaces between the workpiece and the dies were lubricated to minimize frictional effects. The forging experiments were carried out at 25 C and 120 C, at a constant die-closing velocity of 0.02 mm/s. The forging experiments at 25 C were carried to three different die-displacement levels of 2.8 mm, 4.6 mm and 5.4 mm, while the experiment at 120 C was only carried out to a final die-displacement of 5.4 mm.

For the finite element simulation of such a process, we make use of the symmetry of the geometry and only mesh one-quarter of the geometry, as shown in Fig. 9a. The quarter-circle of the workpiece cross-section is meshed with 976 ABAQUS-CPE4R elements, and the cruciform-die is modeled as a rigid surface. Since the physical experiment was well-lubricated, the contact between the die and the workpiece was modeled as frictionless.

Fig. 9b compares the numerically-predicted and the experimentally-measured, load-unload force versus displacement curves for the cruciform-forging processes at 25 C and 120 C. The agreement between the predicted and the measured force-displacement responses at 25 C for die displacements of 2.8 mm, 4.6 mm, and 5.4 mm is very good, as is the agreement between the prediction and the experimental result for the experiment at 120 C for a die displacement of 5.4 mm.

After unloading, each forged specimen was sectioned, polished, and then photographed. Fig. 10a and Fig. 10b compare the numerically-predicted and the experimentally-measured deformed shapes after unloading the test specimens at 5.4 mm of die displacement for the forgings at 25 C and 120 C. The agreement between numerically-predicted and experimentally-measured deformed geometries is also quite good.

6.2.2 Macro-scale, axisymmetric, hot-forging of Zeonex

Axisymmetric, hot-forging experiments were performed on Zeonex specimens. The axi-symmetric forming operation under consideration converts a cylindrical specimen with a circular cross-section into a specimen with a circular base, a bulged-middle, and a tapered neck. A schematic of a forging experiment is shown in Fig. 11. The Zeonex specimens had an original diameter of 10.16 mm, and were 10.16 mm tall. The split-dies which impart the particular shape to the workpiece were made from hardened tool steel, and (in contrast to the lubricated plane-strain forging experiments for PC) the interfaces between the Zeonex workpiece and the dies were *not lubricated*. The axi-symmetric forging experiments were carried out at 90 C and 120 C, at a constant die-closing velocity of 0.02 mm/s. The forging experiments at 90 C were carried out to a final die-displacement of 4.5 mm, while the experiments at 120 C were carried to two different die-displacement levels of 2 mm and 4.5 mm.

For the finite element simulation of such a process we make use of the axial-symmetry of the geometry, and mesh only a slice of the geometry, as shown in Fig. 12a. The workpiece was meshed with 802 ABAQUS-

CAX4R elements, and the top and bottom forging dies were modeled as rigid surfaces; the axis of symmetry is labelled in Fig. 12a. Since no lubricant was used in the physical experiment, the contact between the die and the workpiece was modeled as “rough” with full-sticking.

Fig. 12b compares the numerically-predicted and the experimentally-measured, load-unload force versus displacement curves for the axisymmetric-forging processes at 90 C and 120 C. The fact that numerically-predicted loads are slightly higher than the experimentally-measured loads is to be expected because the numerical simulation assumed perfect-sticking, while in the physical experiment the frictional conditions are less severe. Given the uncertainty in the precise frictional conditions at the interface between the dies and the workpiece in the physical experiment, the agreement between the predicted and the measured load-displacement responses at both temperatures is quite reasonable.

After unloading, the specimens that were forged at 120 C to die-displacement levels of 2 mm and 4.5 mm. were photographed. Fig. 13 compares the numerically-predicted and the experimentally-measured deformed shapes after die-displacements of 2 mm and 4.5 mm. The numerically-predicted shapes are quite similar to those which were experimentally-measured.

6.2.3 Micro-scale hot-embossing of Zeonex

As a simple example of a micro-hot-embossing process, we consider the embossing of a series of long channels into a Zeonex substrate. The pattern consists of channels which are $55\ \mu\text{m}$ wide, $43.5\ \mu\text{m}$ deep, and are spaced $92\ \mu\text{m}$ apart. To carry out the micro-hot-embossing in the polymer, a Zr-based metallic-glass tool with a negative of the desired channel pattern was manufactured by micro-scale thermoplastic forming (Henann and Anand, 2008). Fig. 14a shows a schematic of the pattern of the tool, and Fig. 14b shows a SEM photomicrograph of a portion of the metallic glass tool.

The hot-embossing experiment was carried out on a servo-hydraulic Instron testing machine equipped with heated compression platens. A 25.4 mm square and 2 mm thick sheet of Zeonex, and a 11.7 mm square patterned metallic glass tool were aligned and placed between the heated compression platens. The embossing experiment was conducted under nominally isothermal conditions at a temperature of 130 C in air. The load was ramped up to 13 kN to produce a nominal pressure of 95 MPa in 10 seconds, and held for 2 minutes before unloading, after which the tool was quickly removed from the substrate. The force-cycle for the micro-hot-embossing process is schematically shown in Fig. 15a.

Since the channels are long relative to their width, and there are a large number of them aligned in parallel, we employ a plane-strain idealization in our numerical simulation, and consider only a single half-segment, with suitable boundary conditions. Fig. 15b shows the finite element mesh. The Zeonex substrate is modeled using a mesh consisting of 849 ABAQUS-CPE4R plane strain elements, and the metallic glass tool is modeled using an appropriately shaped rigid surface. Contact between the substrate and tool was approximated as frictionless. The displacement boundary conditions on the portions AD and BC of the mesh boundary are $u_1 = 0$, while on the portion CD of the mesh, $u_1 = u_2 = 0$ are prescribed. The predicted embossed pattern in the Zeonex after hot-embossing is shown in Fig. 15c. The numerically-predicted pattern shown in Fig. 15c has been mirrored and repeated during post-processing to ease comparison with the corresponding experimental result, which is shown Fig. 15d. The final geometry of the embossed channels predicted by the simulations agrees well with the result from the micro-hot-embossing experiment. The simulation, Fig. 15c, predicts that at the embossing temperature of 130 C and nominal pressure of 95 MPa, the micro-hot-embossing should result in channel heights which are the same as the depths in the embossing tool, but there is incomplete die-filling and the edges of the channels are rounded; this is also the result seen in the physical experiment, Fig. 15d.²¹

We further investigated the quality of the embossed features by using optical profilometry methods. Figure 15e compares representative cross-sections of the embossed features in the Zeonex (circles), against the numerically-predicted channel profile (dashed line). The depth of the embossed features closely match with the numerical prediction; note that the optical profilometry method that we used to measure the channel profile is not capable of providing data for the sharp vertical features.

²¹In order to get complete die-filling, it would be ideal to conduct the hot-embossing at temperatures above the glass transition temperature of the polymer, a regime that is of considerable practical interest for the manufacture of microfluidic devices by micro-hot-embossing.

6.3 Normal impact of a clamped circular plate of PC by a spherical-tipped cylindrical projectile

As a final validation experiment — one which is not quasi-static, conducted at high strain rates, and is not isothermal — we consider the normal impact of a circular plate of PC with a spherical-tipped cylindrical projectile. Experiments of this type are of substantial practical interest in the design and testing of *transparent lightweight armor*.

The circular plate specimen of PC, 203.2 mm in diameter and 5.334 mm thick (with bolt-holes for clamping), was fabricated using a water-jet machine. The PC plate was clamped (using steel clamping plates and bolts) in an Instron Dynatup testing machine, and subjected to normal impact by a spherical-tipped cylindrical steel projectile with a mass of 80 kg at an impact velocity of 3.6 m/s. The impact conditions were specially chosen such that the plate only deforms plastically at the high rates, and does not fracture. The force versus time was recorded during the impact, and the impacted plate specimen was recovered.

For the finite element simulation we make use of the axial-symmetry of the geometry, and mesh only a slice of the geometry, as shown in Fig. 16. The PC plate is modeled using 304 ABAQUS-CAX4RT reduced-integration, thermo-mechanically-coupled, axisymmetric elements. The actual clamping boundary conditions are modeled by rigid surfaces representing the clamping plates, but instead of individual clamping bolts, the surface interaction between the rigid surfaces representing the clamping plates and the PC plate is modeled using a high Coulomb friction coefficient of 0.75; thus the polymer is not completely constrained to remain in contact with the clamping surfaces. The spherical-tipped cylindrical steel projectile is modeled as a rigid body with a mass of 80 kg, and given an initial velocity of 3.6 m/s towards the plate specimen. The projectile/polymer interface is modeled as frictionless.

Fig. 17a shows an image of a sectioned one-half the specimen after the experiment, while Fig. 17b shows the corresponding numerically-predicted result. The predicted deformed profile of the polycarbonate plate is qualitatively very similar to that in the experiment. More quantitatively, Fig. 17c shows a comparison of the traced surface profile of the specimen after impact with the numerically calculated profile — the two compare very favorably. Fig. 18a shows the excellent agreement between the experimentally measured, and the simulated force-time response on the projectile — up to the time for which the experimental data was available. Lastly, Fig. 18b shows the temperature distribution in the plate 25 ms after the impact, when the projectile has rebounded and lost contact with the plate. As expected, the temperature rise is largest under the tip of the projectile, where it increases by approximately 45 K, from 298 K to 343 K.

7 Concluding Remarks

We have developed a thermo-mechanically-coupled theory for large deformations of amorphous polymers. A specialized version of the theory has been shown to perform well in reproducing the major intrinsic features of the macroscopic stress-strain response of three representative materials: PMMA, PC, and Zeonex. The thermo-mechanically-coupled theory has been implemented in the finite element program ABAQUS/Explicit (2007). The predictive capabilities of the constitutive theory and its numerical implementation have been validated by comparing the results from a suite of validation experiments of some key macroscopic features, such as the experimentally-measured deformed shapes and the load-displacement curves, against corresponding results from the numerical simulations.

Some important extensions of the theory that remain to be carried out are:

1. To extend the theory to model the large-deformation response of amorphous polymeric materials in a temperature range spanning their glass transition temperatures. Such theories are still in their infancy (e.g., Buckley and Jones, 1995; Dooling et al., 2002; Boyce et al., 2000; Dupaix, 2003; Dupaix and Boyce, 2007). What is needed in this temperature range is a unified constitutive framework to model the transition from a visco-elastic-plastic solid-like response below the glass transition temperature, to a rubbery-viscoelastic response above the glass transition temperature of the material. We will present such an extension in a forthcoming paper.
2. To extend the theory to account for crazing and cavitation and to include suitable damage and failure criteria (cf., e.g., Gearing and Anand, 2004a,b).

When suitably extended, the theory should be useful not only for modeling of fracture initiation from cracks and notches under high-rate loading, but also for modeling and simulation of a variety of polymer processing operations, and for predicting the relationship between processing methods and the subsequent mechanical properties of amorphous polymeric products.

Acknowledgements

This work was supported by the National Science Foundation under grant number DMI-0517966, and the MST program of the Singapore-MIT Alliance. We are grateful to Mr. David Henann of our Laboratory for providing the metallic-glass micro-hot-embossing die. Access to the Instron-Dynatup impact tester in the Impact and Crashworthiness Laboratory at MIT was provided by Professor Tomasz Wierzbicki; the help of Mr. Carey Walters and Miss Emily Houston in conducting the impact experiments is gratefully acknowledged. Discussions with Professor A. S. Argon concerning the free-volume concept and its role in strain-softening of amorphous materials are gratefully acknowledged.

References

- Abaqus/Explicit, 2007. SIMULIA, Providence, RI.
- Anand, L., 1979. On H. Hencky's approximate strain-energy function for moderate deformations. *ASME Journal of Applied Mechanics* **46**, 78-82.
- Anand, L., 1986. Moderate deformations in extension-torsion of incompressible isotropic elastic materials. *Journal of the Mechanics and Physics of Solids* **34**, 293-304.
- Anand, L., and Gu, C., 2000. Granular materials: constitutive equations and strain localization. *Journal of the Mechanics and Physics of Solids*, **48**, 1710-1733.
- Anand, L., and Gurtin, M.E., 2003. A theory of amorphous solids undergoing large deformations, with applications to polymeric glasses. *International Journal of Solids and Structures* **40**, 1465-1487.
- Anand, L., and Ames, N. M., 2006. On modeling the micro-indentation response of an amorphous polymer. *International Journal of Plasticity* **22**, 1123-1170.
- Anand, L., Ames, N. M., Srivastava, V., and Chester, S., 2008. A thermo-mechanically-coupled theory for large deformations of amorphous polymers. Part 1: formulation. *International Journal of Plasticity*, submitted.
- Argon, A.S., 1973. A theory for the low temperature plastic deformation of glassy polymers. *Philosophical Magazine* **28**, 839-865.
- Argon, A.S., and Demkowicz, M.J., 2008. What can plasticity of amorphous silicon tell us about plasticity of metallic glasses? *Metallurgical and Materials Transactions A* **39A**, 1762-1778.
- Armstrong, P. J., and Frederick, C. O., 1966. A mathematical representation of the multiaxial Bauschinger effect. Report RD/B/N731, CEGB, Central Electricity Generating Board, Berkeley, UK.
- Arruda, E. M., and Boyce, M.C., 1993. Evolution of plastic anisotropy in amorphous polymers during finite straining. *International Journal of Plasticity* **9**, 697-720.
- Arruda, E.M., Boyce, M.C., and Jayachandran, R., 1995. Effects of strain rate, temperature and thermomechanical coupling on the finite strain deformation of glassy polymers. *Mechanics of Materials* **19**, 193-212.
- Bauwens, J.C., Bauwens-Crowet, C., and Homeś, G., 1969. Tensile yield-stress behavior of poly(vinyl chloride) and polycarbonate in the glass transition region. *Journal of Polymer Science: Part A-2* **7**, 1745-1754.
- Bauwens, J.C., 1972. Relation between the compression yield stress and the mechanical loss peak of bisphenol-A-polycarbonate in the β transition range. *Journal of Materials Science* **7**, 577-584.

- Bauwens-Crowet, C., Bauwens, J.C., and Homeś, G., 1969. Tensile yield-stress behavior of glassy polymers. *Journal of Polymer Science: Part A-2* **7**, 735–742.
- Bauwens-Crowet, C., Bauwens, J.C., and Homeś, G., 1972. The temperature dependence of yield of polycarbonate in uniaxial compression and tensile tests. *Journal of Materials Science* **7**, 176183.
- Bauwens-Crowet, C., 1973. The compression yield behaviour of polymethyl methacrylate over a wide range of temperatures and strain-rates. *Journal of Materials Science*, **8**, 968-979.
- Bjerke, T., Li, Z., and Lambros, J., 2002. Role of plasticity in heat generation during high rate deformation and fracture of polycarbonate. *International Journal of Plasticity* **18**, 549-567.
- Bicerano, J., 1993. *Prediction of Polymer Properties*. Marcel Dekker Inc., New York.
- Boyce, M.C., Parks, D.M., and Argon, A. S., 1988. Large inelastic deformation of glassy polymers. Part 1: rate dependent constitutive model. *Mechanics of Materials* **7**, 15-33.
- Boyce, M. C., 1996. Direct comparison of the Gent and the Arruda-Boyce constitutive models of rubber elasticity. *Rubber Chemistry and Technology* **69**, 781-785.
- Boyce, M.C., Socrate, S., and Llana, P.G., 2000. Constitutive model for the finite deformation stress-strain behavior of poly(ethylene terephthalate) above the glass transition. *Polymer* **41**, 2183-2201.
- Bronkhorst, C.A., Kalidindi, S.R., and Anand, L., 1992. Polycrystalline plasticity and the evolution of crystallographic texture in fcc metals. *Philosophical Transactions of The Royal Society of London A* **341**, 443–477.
- Buckley, C. P., and Jones D. C., 1995. Glass-rubber constitutive model for amorphous polymers near the glass transition. *Polymer* **36**, 3301-3312.
- Chaboche, J. L., 2008. A review of some plasticity and viscoplasticity constitutive theories. *International Journal of Plasticity*. doi: 10.1016/j.ijplas.2008.03.009
- Cohen, M.H., and Grest, G.S., 1979. Liquid-glass transition, a free volume approach. *Physical Review B* **20**, 1077–1098.
- Crist, B., 1997. Yield processes in glassy polymers. In *The Physics of Glassy Polymers* 2nd Ed. Haward, R. N., Young, R. J., Chapman & Hall, London, pp. 155-212.
- Dooling, P. J., Buckley, C. P., Rostami, S., and Zahalan, N., 2002. Hot-drawing of poly(methyl methacrylate) and simulation using a glass-rubber constitutive model, *Polymer* **43**, 2451-2465.
- Dupaix, R. B., 2003. Temperature and rate dependent finite strain behavior of poly(ethylene terephthalate) and poly(ethylene terephthalate)-glycol above the glass transition temperature. *PhD Dissertation*, Massachusetts Institute of Technology.
- Dupaix, R. B. and Boyce, M. C., 2007. Constitutive modeling of the finite strain behavior of amorphous polymers in and above the glass transition. *Mechanics of Materials* **39**, 39-52.
- Eyring, H., 1936. Viscosity, plasticity, and diffusion as examples of absolute reaction rates. *Journal of Chemical Physics* **4**, 283–291.
- Fotheringham, D.G., and Cherry, B.W., 1976. Comment on the compression yield behaviour of polymethyl methacrylate over a wide range of temperatures and strain-rates. *Materials Science Letters* **11**, 1368-1371.
- Fotheringham, D.G., and Cherry, B.W., 1978. The role of recovery forces in the deformation of polyethylene. *Journal of Materials Science* **13**, 951-964.
- Gearing, B. P., and Anand, L., 2004a. Notch-sensitive fracture of polycarbonate *International Journal of Solids and Structures* **41**, 827-845.
- Gearing, B. P., and Anand, L., 2004b. On modeling the deformation and fracture response of glassy polymers due to shear-yielding and crazing. *International Journal of Solids and Structures* **41** 3125-3150.
- Garg, M., Mulliken, A. D., and Boyce, M., 2008. Temperature rise in polymeric materials during high rate deformation, *Journal of Applied Mechanics*, **75**, 011009 (8 pages).

- Gent, A. N., 1996. A new constitutive relation for rubber. *Rubber Chemistry and Technology* **69**, 59-61.
- Henann, D., and Anand, L., 2008. A constitutive theory for the mechanical response of amorphous metals at high temperatures spanning the glass transition temperature: application to microscale thermoplastic forming. *Acta Materialia* **56**, 3290–3305.
- Kröner, E., 1960. Allgemeine kontinuumstheorie der versetzungen und eigenspannungen. *Archive for Rational Mechanics and Analysis* **4**, 273-334.
- Mulliken, A.D., and Boyce, M. C., 2006. Mechanics of the rate-dependent elastic-plastic deformation of glassy polymers from low to high strain rates. *International Journal of Solids and Structures* **43**, 1331–1356.
- Parks, D. M., Argon, A. S., and Bagepalli, B., 1985. Large elastic-plastic deformation of glassy polymers, part 1: Constitutive modelling. Report, MIT, Program in Polymer Science and Technology.
- Povolo, F., and Hermida, E.B., 1995. Phenomenological description of the strain rate and temperature-dependent yield stress of PMMA. *Journal of Applied Polymer Science* **58**, 55-68.
- Povolo, F., and Hermida, E.B., 1996. Temperature and strain rate dependence of the tensile yield stress of PVC. *Journal of Applied Polymer Science* **61**, 109-117.
- Richeton, J., Ahzi, S., and Daridon, L. Rémond, Y., 2005. A formulation of the cooperative model for the yield stress of amorphous polymers for a wide range of strain rates and temperatures. *Polymer* **46**, 6035-6043
- Richeton, J., Ahzi, S., Vecchio, K.S., Jiang, F.C., and Adharapurapu, R.R., 2006. Influence of temperature and strain rate on the mechanical behavior of three amorphous polymers: characterization and modeling of the compressive yield stress. *International Journal of Solids and Structures* **43**, 2318-2335.
- Richeton, J., Ahzi, S., Vecchio, K.S., Jiang, F.C., and Makardi, A., 2007. Modeling and validation of the large deformation inelastic response of amorphous polymers over a wide range of temperatures and strain rates. *International Journal of Solids and Structures* **44**, 7938-7954.
- Robertson, R. E., 1966. Theory for the plasticity of glassy polymers. *Journal of Chemical Physics* **44**, 3950-3956.
- Shah, V. M., Stern, S.A., and Ludovice, P. J., 1989. Estimation of the free volume in polymers by means of a Monte Carlo technique. *Macromolecules* **22**, 4660–4662.
- Swift, H. W., 1947. Length changes in metals under torsional overstrain. *Engineering* **163**, 253–257.
- Van Krevelen, D.W., 1990. *Properties of Polymers*, third ed. Elsevier, Amsterdam.
- Wu, P. D., and Van der Giessen, E., 1993a. On improved network models for rubber elasticity and their applications to orientation hardening of glassy polymers. *Journal of the Mechanics and Physics of Solids* **41**, 427-456.
- Wu, P. D., and Van der Giessen, E., 1993b. On large strain inelastic torsion of glassy polymers. *International Journal of Mechanical Sciences* **35**, 935–951.

8 Appendix: calibration of material parameters in the constitutive model

In this appendix we briefly outline a heuristic procedure for estimating values of the material parameters in the constitutive model. As an example, the procedure is applied to determine the material parameters for the amorphous polymer Zeonex. For an isotropic theory such as the one presented in this paper, it is most convenient to use an implementation of a one-dimensional version of our model (described below) in the computer program MATLAB to conduct appropriate simulations to estimate the material parameters.

8.1 One-dimensional version of the constitutive theory

In this section we present an *approximate* one-dimensional version of the model, which substantially aids in the calibration of material properties from experimental data. The approximation is primarily in that we cannot account for Poisson's type lateral contractions, and attendant volume changes, in a one-dimensional setting. The underlying constitutive equations relate the following basic fields:

$U > 0$,	stretch,
U^p ,	plastic stretch,
$U^e = UU^{p-1}$,	elastic part of the stretch,
$\epsilon = \ln U$,	logarithmic strain,
$\epsilon^e = \ln U^e$,	logarithmic elastic strain,
$\boldsymbol{\xi} = (\varphi, S_1, S_2)$	scalar internal variables,
$A > 0$,	squared stretch-like internal variable,
$\vartheta > 0$,	absolute temperature,
$\psi = \psi^{(1)}(U^e, \vartheta) + \psi^{(2)}(U, \vartheta) + \psi^{(p)}(A, \vartheta)$,	free energy density,
σ	Cauchy stress.

8.1.1 Free energy. Stress. Back-stress.

For $\psi^{(1)}$ we use a simple linear elastic form for the free energy

$$\psi^{(1)} = \frac{1}{2} E (\epsilon^e)^2 - E \alpha (\vartheta - \vartheta_0) \epsilon^e + \tilde{f}(\vartheta), \quad (8.1)$$

where $E(\vartheta) > 0$ is Young's modulus, α is the coefficient of thermal expansion, ϑ_0 is a reference temperature, and $\tilde{f}(\vartheta)$ is an entropic contribution to the free energy related to the specific heat of the material. This free energy contributes a component

$$\sigma^{(1)} = E \epsilon^e - E \alpha (\vartheta - \vartheta_0), \quad (8.2)$$

to the total Cauchy stress σ .

For $\psi^{(2)}$, consider first a symmetric positive definite stretch tensor \mathbf{U} which satisfies $\det \mathbf{U} = 1$. Let (U_1, U_2, U_3) denote the set of principal stretches, with $U_1 U_2 U_3 = 1$. The first invariant I_1 of the squared-stretch tensor \mathbf{U}^2 in three-dimensions is defined by

$$I_1 \stackrel{\text{def}}{=} U_1^2 + U_2^2 + U_3^2. \quad (8.3)$$

In terms of I_1 , the Gent (1996) free energy is

$$\psi^{(2)} = -\frac{1}{2} \mu_{\text{R}} I_m \ln \left(1 - \frac{I_1 - 3}{I_m} \right), \quad (8.4)$$

where $\mu_{\text{R}}(\vartheta) > 0$ and $I_m > 3$ are two material parameters, with μ_{R} representing the ground state rubbery shear modulus of the material, and I_m representing the upper limit of $(I_1 - 3)$, associated with limited chain extensibility. With $\sigma^{(2)}$ denoting the contribution to the Cauchy stress from this free energy, standard relations of finite deformation incompressible elasticity give the the principal values of the corresponding stress as

$$\sigma_i^{(2)} = U_i \frac{\partial \psi^{(2)}}{\partial U_i} - P, \quad (8.5)$$

with P an arbitrary "pressure." In simple tension/compression, with $\sigma_1^{(2)} \equiv \sigma^{(2)}$ and $\sigma_2^{(2)} = \sigma_3^{(2)} = 0$, we get

$$\sigma^{(2)} = U_1 \frac{\partial \psi^{(2)}}{\partial U_1} - U_2 \frac{\partial \psi^{(2)}}{\partial U_2} = \frac{\partial \psi^{(2)}}{\partial I_1} \left(U_1 \frac{\partial I_1}{\partial U_1} - U_2 \frac{\partial I_1}{\partial U_2} \right) = 2 \frac{\partial \psi^{(2)}}{\partial I_1} (U_1^2 - U_2^2), \quad (8.6)$$

or equivalently, with $U_1 \equiv U$ and $U_2 = U_3 = U^{-1/2}$,

$$\sigma^{(2)} = 2 \frac{\partial \psi^{(2)}}{\partial I_1} (U^2 - U^{-1}), \quad (8.7)$$

and hence, for the Gent free energy (8.4),

$$\sigma^{(2)} = \mu_R \left(1 - \frac{I_1 - 3}{I_m}\right)^{-1} (U^2 - U^{-1}). \quad (8.8)$$

The total Cauchy stress in simple tension/compression is

$$\sigma = \sigma^{(1)} + \sigma^{(2)}. \quad (8.9)$$

Next, for $\psi^{(p)}$, consider a symmetric positive definite squared-stretch-like tensor \mathbf{A} which satisfies $\det \mathbf{A} = 1$. Let (a_1, a_2, a_3) denote the set of principal values of \mathbf{A} , with $a_1 a_2 a_3 = 1$. We assume a plastic energy of the form

$$\psi^{(p)} = \frac{1}{4} B [(\ln a_1)^2 + (\ln a_2)^2 + (\ln a_3)^2], \quad (8.10)$$

where $B(\vartheta) \geq 0$ is a back-stress modulus. With $\sigma^{(\text{back})}$ denoting a stress from this free energy, standard relations of finite deformation incompressible elasticity give the corresponding principal values of the back-stress as

$$\sigma_i^{(\text{back})} = 2a_i \frac{\partial \psi^{(p)}}{\partial a_i} - P, \quad (8.11)$$

with P an arbitrary ‘‘pressure,’’ so that in a simple tension/compression, with $\sigma_1^{(\text{back})} \equiv \sigma_{\text{back}}$, $\sigma_2^{(\text{back})} = \sigma_3^{(\text{back})} = 0$,

$$\sigma_{\text{back}} = 2a_1 \frac{\partial \psi^{(p)}}{\partial a_1} - 2a_2 \frac{\partial \psi^{(p)}}{\partial a_2}. \quad (8.12)$$

When the free energy is given by (8.10), (8.12) reduces to

$$\sigma_{\text{back}} = B (\ln a_1 - \ln a_2), \quad (8.13)$$

or equivalently, with $a_1 = A$, and $a_2 = a_3 = A^{-1/2}$,

$$\sigma_{\text{back}} = \frac{3}{2} B \ln A. \quad (8.14)$$

In a one-dimensional setting, the driving stress for plastic flow is the effective stress given by

$$\sigma_{\text{eff}}^{(1)} = \sigma^{(1)} - \sigma_{\text{back}}, \quad (8.15)$$

and the *equivalent tensile stress* and the *mean normal pressure* are

$$\bar{\sigma} \stackrel{\text{def}}{=} |\sigma_{\text{eff}}^{(1)}| \quad \text{and} \quad \bar{p} = -\frac{1}{3} \sigma^{(1)}, \quad (8.16)$$

respectively.

8.1.2 Flow rule

The evolution equation for U^p is

$$\left. \begin{aligned} \dot{U}^p &= D^p U^p & U^p(0) &= 1, \\ D^p &= \dot{\epsilon}^p \text{sign}(\sigma^{(1)}), & \dot{\epsilon}^p &\geq 0, \\ \sigma_e &\stackrel{\text{def}}{=} \bar{\sigma} - (S_1 + S_2 + \alpha_p \bar{p}), \\ \dot{\epsilon}^p &= \begin{cases} 0 & \text{if } \sigma_e \leq 0, \\ \dot{\epsilon}_0 \exp\left(-\frac{Q}{k_B \vartheta}\right) \left[\sinh\left(\frac{\sigma_e V}{2 k_B \vartheta}\right)\right]^{1/m} & \text{if } \sigma_e > 0. \end{cases} \end{aligned} \right\} \quad (8.17)$$

Here $\dot{\epsilon}^p$ is the *equivalent tensile plastic strain-rate*, and σ_e denotes a *net equivalent tensile stress for thermally activated flow*; α_p is a pressure-sensitivity parameter; $\dot{\epsilon}_0$ is a *pre-exponential factor* with units of s^{-1} ; Q is an

activation energy; k_B is Boltzmann's constant; V is an activation volume; and m is a strain rate sensitivity parameter.

When $\dot{\epsilon}^p > 0$, (8.17), using (8.15) and (8.16), may be inverted to give

$$|\sigma^{(1)} - \sigma_{\text{back}}| + \frac{1}{3}\alpha_p \sigma^{(1)} = S_1 + S_2 + \frac{2k_b\vartheta}{V} \sinh^{-1} \left[\left(\frac{\dot{\epsilon}^p}{\dot{\epsilon}^*(\vartheta)} \right)^m \right], \quad (8.18)$$

with

$$\dot{\epsilon}^*(\vartheta) \stackrel{\text{def}}{=} \dot{\epsilon}_0 \exp\left(-\frac{Q}{k_B\vartheta}\right). \quad (8.19)$$

8.1.3 Evolution equations for the internal variables S_1 , φ , S_2 , and A

The internal variables S_1 and φ are taken to obey the coupled evolution equations:

$$\dot{S}_1 = h_1 (S_1^* - S_1) \dot{\epsilon}^p, \quad \text{with } S_1^* = b(\varphi^* - \varphi), \quad \text{and } S_1(0) = S_{1i}; \quad (8.20)$$

and

$$\left. \begin{aligned} \dot{\varphi} &= g(\varphi^* - \varphi) \dot{\epsilon}^p, & \text{with } \varphi(0) &= \varphi_i, \\ \text{and } \varphi^*(\dot{\epsilon}^p, \vartheta) &= \begin{cases} \varphi_r \left[1 + \left(\frac{\vartheta_c - \vartheta}{k} \right)^r \right] \left(\frac{\dot{\epsilon}^p}{\dot{\epsilon}_r} \right)^s & \text{for } \vartheta \leq \vartheta_c, \\ 0 & \text{for } \vartheta > \vartheta_c, \end{cases} \\ \text{where } \vartheta_c &= \begin{cases} \vartheta_g + n \ln \left(\frac{\dot{\epsilon}^p}{\dot{\epsilon}_r} \right) & \text{for } \dot{\epsilon}^p > \dot{\epsilon}_r, \\ \vartheta_g & \text{for } \dot{\epsilon}^p \leq \dot{\epsilon}_r, \end{cases} \end{aligned} \right\} \quad (8.21)$$

with $\{h_1, b, S_{1i}, \varphi_i, \varphi_r, k, r, s, \dot{\epsilon}_r, n\}$ constants, and g temperature-dependent.

The evolution of S_2 is taken to be governed by

$$\dot{S}_2 = h_2 (\bar{\lambda}^p - 1) (S_2^* - S_2) \dot{\epsilon}^p, \quad \text{with initial value } S_2(0) = S_{2i} \geq 0, \quad (8.22)$$

where

$$\bar{\lambda}^p \stackrel{\text{def}}{=} \sqrt{(U^p)^2 + 2U^{p-1}}/3 \quad (8.23)$$

is an effective plastic stretch, h_2 a constant, and S_2^* temperature-dependent.

Also, the evolution equation for A is taken as

$$\dot{A} = 2A D^p - \gamma(A \ln A) \dot{\epsilon}^p, \quad A(0) = 1, \quad (8.24)$$

where $\gamma \geq 0$ is a constitutive parameter which governs the dynamic recovery of A .

8.1.4 Evolution equation for temperature

For one-dimensional tests at the highest strain rates, which may be approximated as adiabatic, the temperature is taken to evolve according to

$$c\dot{\vartheta} = \omega \left(\sigma_e + \frac{1}{2} B \gamma |\ln A|^2 \right) \dot{\epsilon}^p. \quad (8.25)$$

8.2 Material parameter calibration

With the full three-dimensional and simplified one-dimensional version of the theory in place, we are in position to estimate the material parameters/functions appearing in the theory by fitting the experimental data. We illustrate our heuristic material parameter calibration procedure for Zeonex; the procedure for PMMA and PC is essentially identical.

We have implemented the one-dimensional model of Section 8.1 in MATLAB using an explicit integration scheme, and we use it to calibrate the material parameters from the experiments described in §2. The one-dimensional calibration process consists of four sequential steps which are outlined in this section. The four steps cover calibration of the following aspects of the stress-strain response: (1) elastic modulus; (2) initial yield stress; (3) large strain behavior; and (4) yield-peak and back-stress.

8.2.1 Elastic modulus

For polymeric materials the magnitude of the Young's modulus E decreases as the temperature increases. We assume that the temperature dependence of the Young's modulus may be adequately approximated by (cf. (4.90))²²

$$E(\vartheta) = E_0 - M_E(\vartheta - \vartheta_g),$$

where E_0 and M_E are constants. Using the experimental data for the E versus ϑ , we estimate

$$E_0 = 1350 \text{ MPa}, \quad M_E = 0.45 \text{ MPa K}^{-1}.$$

8.2.2 Initial yield stress

Most previous models for amorphous polymers have identified the *peak stress* in a stress-strain curve from a simple compression test as a “yield stress” for the material. Since the stress-peak is associated with the transient disordering of the material, and the actual level of a peak is very dependent on the initial thermal history of the material, here we follow a different approach. We identify a “yield stress” in a compression experiment as a back-extrapolated value of the intersection of the initial elastic slope with the tangent to the stress-strain curve at a strain of, say, 0.4, a strain level by which all transients of the yield-peak have died out, and the chain-locking effects giving rise to the stress-strain curve are minimal. Accordingly, at this point in the calibration procedure we ignore the effects of the yield-peak and define the “yield stress” as the intersection of the pre-peak stress-strain curve with the back-extrapolated tangent to the stress-strain curve at approximately 0.4 strain; this is shown schematically in Fig. 19.²³

Since

$$|\sigma^{(1)} - \sigma_{\text{back}}| = (\sigma^{(1)} - \sigma_{\text{back}}) \text{sign}(\sigma^{(1)} - \sigma_{\text{back}})$$

and since in a monotonic compression test

$$\text{sign}(\sigma^{(1)} - \sigma_{\text{back}}) = \text{sign}(\sigma^{(1)}) = \text{sign}(\sigma_{\text{back}}),$$

we have

$$|\sigma^{(1)} - \sigma_{\text{back}}| = |\sigma^{(1)}| - |\sigma_{\text{back}}|,$$

and hence, from (8.18),

$$\left(1 - \frac{\alpha_p}{3}\right) |\sigma^{(1)}| = S_1 + S_2 + |\sigma_{\text{back}}| + \frac{2k_b\vartheta}{V} \sinh^{-1} \left[\left(\frac{\dot{\epsilon}^p}{\dot{\epsilon}^*(\vartheta)} \right)^m \right]. \quad (8.26)$$

Thus, neglecting the contribution from the internal variables S_1 (which is associated with the transient yield peak) and the contribution from S_2 (since this only manifests itself at large stretches), for fully-developed flows when $\dot{\epsilon}^p \approx \dot{\epsilon}$ (taken to be positive in compression) and with $|\sigma^{(1)}| = \sigma_y$, (8.26) gives the following approximate expression for yield stress σ_y as a function of temperature ϑ and strain rate $\dot{\epsilon}$:

$$\left(1 - \frac{\alpha_p}{3}\right) \sigma_y \approx \sigma_{\text{back}}^*(\vartheta) + \frac{2k_B\vartheta}{V} \sinh^{-1} \left[\left(\frac{\dot{\epsilon}}{\dot{\epsilon}^*(\vartheta)} \right)^m \right], \quad (8.27)$$

where we have introduced the notation

$$\sigma_{\text{back}}^*(\vartheta) \stackrel{\text{def}}{=} |\sigma_{\text{back}}(\vartheta)|. \quad (8.28)$$

Here, $\sigma_{\text{back}}^*(\vartheta)$ represents a temperature-dependent *saturation value* of the back-stress in compression.²⁴ Because of the assumed temperature dependence (4.92) of the back-stress modulus, σ_{back}^* decreases linearly with temperature,

$$\sigma_{\text{back}}^* = R(\vartheta_g - \vartheta) \quad \text{for } \vartheta \leq \vartheta_g, \quad (8.29)$$

²²We ignore all rate-sensitivity of the initial stiffness.

²³This is a non-standard definition of the yield stress for polymeric materials.

²⁴For the purpose of obtaining material parameters associated with the “yield stress,” we ignore the evolution of the back-stress and use the temperature-dependent *saturation value* for the back-stress as an internal stress in the one-dimensional theory. In order to make connection with the work of Richeton et al. (2005, 2006, 2007), one may identify $\sigma_{\text{back}}^*(\vartheta)$ with their internal stress $\sigma_i(\vartheta)$. Note, however, that in the work of Richeton et al., $\sigma_i(\vartheta)$ is always a positive valued scalar internal stress which leads to isotropic hardening, whereas in our more general theory the back-stress may in general be positive or negative, and is not only temperature dependent, but also evolves with strain to give rise to kinematic hardening.

where R is a material parameter. Finally, recalling (8.19),

$$\dot{\epsilon}^*(\vartheta) \stackrel{\text{def}}{=} \dot{\epsilon}_0 \exp\left(-\frac{Q}{k_B\vartheta}\right). \quad (8.30)$$

To summarize, from (8.27), (8.29), and (8.30), there is a list of six material parameters

$$\{\alpha_p, V, m, R, \dot{\epsilon}_0, Q\} \quad (8.31)$$

that must be calibrated from the experimental data for σ_y as a function of strain rate $\dot{\epsilon}$ and temperature ϑ . The value of the pressure-sensitivity parameter α_p is not determinable from simple compression experiments alone. As reviewed by Crist (1997), for amorphous polymers the pressure-sensitivity parameter α_p in simple tension/compression for PMMA is ≈ 0.35 , that for PC is ≈ 0.2 , and for amorphous polymers is generally in the range 0.1 to 0.4. We are not aware of any data for the pressure sensitivity of yield for Zeonex in the literature. Here, we assume that

$$\alpha_p \approx 0.2 \quad (8.32)$$

for Zeonex. This reduces the list (8.31) to

$$\{V, m, R, \dot{\epsilon}_0, Q\}, \quad (8.33)$$

which need to be calibrated from the experimental data for σ_y as a function of strain rate $\dot{\epsilon}$ and temperature ϑ .

Following the back-extrapolation method of Fig. 19, values of the yield stress σ_y as a function of temperature ϑ and strain rate $\dot{\epsilon}$ have been estimated from the compression stress-strain curves for Zeonex in the temperature range 25 C to 130 C at four strain-rates. The ratio of these yield stresses to test temperatures, σ_y/ϑ , as a function of the logarithm of strain-rate, $\log_{10} \dot{\epsilon}$ are shown in the Eyring-plot of Fig. 20a. Estimated isotherms have been drawn to visually connect the yield points for a given test temperature. For a given temperature we have only four data points spanning a relatively narrow strain-rate range, which makes fitting the flow function (8.27) difficult. However, by utilizing the shifting and superposition ideas of Richeton et al. (2005b, 2006), we can form a master curve of all 16 data points at a single reference temperature that covers a much wider range of strain rates. To obtain the master curve, the experimental data is shifted along both axes by temperature-dependent shift factors defined below:

$$\left. \begin{aligned} \text{Horizontal shift:} \quad \Delta(\log_{10} \dot{\epsilon}) &= H_h \left(\frac{1}{\vartheta} - \frac{1}{\vartheta_{\text{shift}}} \right), \\ \text{Vertical shift:} \quad \Delta \left(\frac{\sigma_y}{\vartheta} \right) &= H_v \left(\frac{1}{\vartheta} - \frac{1}{\vartheta_{\text{shift}}} \right), \end{aligned} \right\} \quad (8.34)$$

where ϑ is the temperature of the experiment, ϑ_{shift} is the temperature that the data is shifted to, and H_h and H_v are shift parameters. Richeton et al. (2005b, 2006) have argued that these shift factors may be equated with the material parameters appearing in the cooperative flow model such that

$$\left. \begin{aligned} H_h &= \frac{Q}{k_B \ln 10}, \\ H_v &= -\sigma_{\text{back}}^*(\vartheta = 0) = -R\theta_g. \end{aligned} \right\} \quad (8.35)$$

The master curve constructed at $\vartheta_{\text{shift}} = \vartheta_g = 408$ K using the shift factors

$$H_h = 5.7 \times 10^3 \text{ K}, \quad H_v = -70 \text{ MPa},$$

is shown in Fig. 20b, and the values of Q and R , calculated using (8.35), are

$$Q = 1.81 \times 10^{-19} \text{ J}, \quad \text{and} \quad R = 0.172 \text{ MPa K}^{-1}.$$

For a master curve constructed at $\vartheta_{\text{shift}} = \vartheta_g$, the back-stress term from the flow function (8.27) vanishes, and (8.27) simplifies to

$$\frac{\sigma_y}{\vartheta_g} = \frac{2k_B}{V} \left(1 - \frac{\alpha_p}{3}\right)^{-1} \sinh^{-1} \left[\left(\frac{\dot{\epsilon}}{\dot{\epsilon}^*(\vartheta_g)} \right)^m \right], \quad (8.36)$$

with the list of unknown parameters reduced to $\{\dot{\epsilon}_0, V, m\}$. A non-linear least-squares fitting method was used in MATLAB to obtain these parameters from the shifted experimental data. This gives

$$\dot{\epsilon}_0 = 1.8 \times 10^{11} \text{ s}^{-1}, \quad V = 1.14 \times 10^{-27} \text{ m}^3, \quad \text{and} \quad m = 0.16,$$

and the resulting fit of (8.36) to the shifted data at 408K is shown in Fig. 20b as a solid line.

8.2.3 Stress-strain response at large strains

Here, we focus on estimating the material parameters: (1) μ_R and I_m in the expression (8.8), together with the temperature dependence of μ_R given in (4.95); and (2) h_2 and S_2^* , together with the temperature dependence of S_2^* given in (4.94) — parameters which account for the stress increase associated with chain-locking at large stretches.

To begin, we neglect the transient response associated with the yield-peak and set $\varphi_i = S_{1i} = 0$, and correspondingly ignore the evolution equations (8.20) and (8.21) for φ and S_1 ; we return to determining the material parameters appearing in these coupled evolution equations later. We also ignore the evolution of the back-stress, and set it constant, using the temperature-dependent saturation value, such that

$$\sigma_{\text{back}}(\vartheta) = \sigma_{\text{back}}^*(\vartheta) \text{sign}(\sigma_{\text{back}}) = -R(\vartheta_g - \vartheta) \quad \text{for} \quad \vartheta < \vartheta_g, \quad (8.37)$$

and determine material parameters associated with the evolution of the back-stress later.

Below the glass transition temperature, the parameter I_m is presumed to be temperature-independent, as is the parameter h_2 in the evolution equation (8.22), while the temperature-dependence of $\mu_R(\vartheta)$ and $S_2^*(\vartheta)$ is presumed to follow

$$\mu_R(\vartheta) = \mu_0 - N(\vartheta - \vartheta_g) \quad \text{for} \quad \vartheta < \vartheta_g, \quad (8.38)$$

and

$$S_2^*(\vartheta) = l_1 - l_2\vartheta \quad \text{for} \quad \vartheta < \vartheta_g, \quad (8.39)$$

(cf., (4.95) and (4.94)). Using the one-dimensional MATLAB implementation of the model, together with the material parameters estimated to this point, estimates for the desired parameter list

$$\{\mu_0, N, I_m, S_{2i}, h_2, l_1, l_2\}$$

are relatively easily obtained by curve-fitting both the loading as well as the unloading response at large strains for the stress-strain data at the lowest strain rate.²⁵ A few trials give the estimates as

$$\begin{aligned} \mu_0 &= 3 \text{ MPa}, & N &= 6.2 \times 10^{-2} \text{ MPa K}^{-1}, & I_m &= 6.2, \\ h_2 &= 6.24, & l_1 &= 130 \text{ MPa}, & l_2 &= 0.27 \text{ MPa K}^{-1}. \end{aligned}$$

8.2.4 Yield-peak and back-stress evolution

Finally we calibrate material parameters associated with the yield-peak and the back-stress evolution. This last step in the calibration procedure is an iterative process, and requires fitting the transient stress-overshoot in the simple compression stress-strain response together with the creep response, iteratively, several times in order to get a good fit. The steps in the iterative procedure are listed below.

Step 1:

The parameters related to the change of back-stress σ_{back} with strain and temperature are γ and X (cf. (8.24), (4.92)). To begin, we note that for compression

$$D^p = -\dot{\epsilon}^p, \quad (8.40)$$

²⁵The internal variable S_2 , together with its evolution (8.22), is essential for a proper modeling of the unloading response of the material after large strains. We assume that the material begins in a well-annealed, “ground” state and take S_{2i} to be zero. For PMMA the experimental data, to which the model is fit, to does not include data at very large strains, therefore we ignore the material parameters associated with the isotropic hardening at large strains and set h_2, l_1, l_2 to be zero for this material.

and we may then rewrite the evolution equation for A (8.24) as

$$\dot{A} = -(2 + \gamma \ln A) A \dot{\epsilon}^p. \quad (8.41)$$

It follows then that the saturation value of A in compression is

$$A^* = \exp\left(-\frac{2}{\gamma}\right). \quad (8.42)$$

Combining this result with the equation for the back-stress (8.14) gives the saturation value of the back-stress as a function of the material parameters $B(\vartheta)$ and γ

$$\sigma_{\text{back}}^*(\vartheta) = 3 \frac{B(\vartheta)}{\gamma}. \quad (8.43)$$

Equating the saturation value for the back-stress using (4.92) and (8.29)₁ we obtain

$$3 \frac{X(\vartheta_g - \vartheta)}{\gamma} = R(\vartheta_g - \vartheta) \quad \Rightarrow \quad X = \frac{R}{3} \gamma, \quad (8.44)$$

and since R has already been determined, we obtain the fixed value for the ratio X/γ .

Step 2:

In this step we estimate a value for γ , and calculate the corresponding value for X from (8.44) to get an estimate for the parameters involved in the evolution of the back-stress. This leaves one with a list of parameters $\{S_{1i}, h_1, b, \varphi_i, g, \varphi^*\}$ in the evolution equations (8.20) and (8.21) for φ and S_1 to calibrate the yield-peak.

We assume the material begins in a well-annealed “ground-state,” so that we may take the initial value of the order parameter φ and stress like internal resistance S_1 to be zero,

$$\varphi_i = 0 \quad \text{and} \quad S_{1i} = 0.$$

To find $\{h_1, b, g, \varphi^*\}$, several simulations are performed using different values of parameters to approximately match the shape of the yield peak at the various strain rates and temperatures. As an aid to the iterative curve-fitting procedure, Fig. 21 shows how the parameters $\{h_1, b, g, \varphi^*\}$ affect the shape of the yield-peak. The parameter h_1 controls the initial slope of the yield peak, the parameters b and φ^* control the height of the yield peak, while the parameter g controls the width of the yield-peak.

Step 3:

With the parameters for yield-peak estimated, one returns to refining the values of the material parameters in the back-stress evolution. To get refined estimates for the recovery parameter γ and the temperature sensitivity parameter X for the back-stress modulus B , we first note that γ controls the rate of saturation of the back-stress. This is shown in Fig. 22a, where the back-stress versus axial strain response is shown for varying values of γ at a constant ratio of B/γ : as γ increases, the back-stress approaches its saturation value more rapidly.

The parameters γ and B significantly affect the creep response of the material.²⁶ In order to get more refined estimates for these parameters, we turn to a limited set of available data for room-temperature creep of Zeonex shown in Fig. 22b as solid lines. The value of γ is chosen such that that the creep response is adequately represented, as shown by the dashed lines in Fig. 22b.

Steps 2 and 3 are iteratively repeated until the yield-peaks in the total stress-strain response of the material, as well as the creep response are satisfactorily calibrated.

Once $\{h_1, b, g, \varphi^*\}$ are determined for each stress-strain curve, we have found that to a good approximation, the parameters h_1 and b may be taken as constants; g as temperature dependent, and φ^* as both temperature and strain rate dependent. The temperature dependence of g was then fit to the functional

²⁶Cyclic tension-compression stress-strain curves at different temperatures may also be used to fit the back-stress parameters, but we have not conducted the necessary extensive set of such experiments.

form (4.93), while the temperature and strain rate dependence of φ^* was fit to the functional form (8.21); Fig. 23 shows a schematic of the variation of φ^* with temperature and strain rate.

The material parameters for Zeonex that give a reasonable fit for the yield peak for the range of temperatures and strain rates under consideration, and also adequately reproduce the limited creep data, are

$$\begin{array}{llll}
h_1 = 300, & b = 10.13 \times 10^3 \text{ MPa}, & g_1 = -28, & g_2 = 0.12, \\
\varphi_r = 7.2 \times 10^{-4}, & k = 0.16 \text{ K}, & r = 0.24, & s = 0.045, \\
\nu_r = 3 \times 10^{-4} \text{ s}^{-1} & n = 1.6, & \gamma = 12, & X = 0.7 \text{ MPa K}^{-1},
\end{array}$$

8.3 Parameters for the three-dimensional model

Except for the list of parameters $\{\nu_0, \alpha_p, V, S_{1i}, h_1, b, g_1, g_2, S_{2i}, h_2, l_1, l_2, \nu_r, \gamma\}$, the values of the one-dimensional material parameters are unchanged when used in the three-dimensional equations. Noting that

$$\tau\nu = \sigma\dot{\epsilon}, \quad \sigma = \sqrt{3}\tau, \quad \dot{\epsilon} = \frac{\nu}{\sqrt{3}}, \quad (8.45)$$

the list of parameters $\{\nu_0, \alpha_p, V, S_{1i}, h_1, b, g_1, g_2, S_{2i}, h_2, l_1, l_2, \nu_r, \gamma\}$ may be converted from the one-dimensional compression form to the three-dimensional shear form using

$$\left. \begin{array}{l}
\dot{\epsilon}_0 = \frac{1}{\sqrt{3}} \nu_0, \quad \alpha_p^{(\text{comp})} = \sqrt{3} \alpha_p^{(\text{shear})}, \quad V^{(\text{comp})} = \frac{1}{\sqrt{3}} V^{(\text{shear})}, \\
S_{1i}^{(\text{comp})} = \sqrt{3} S_{1i}^{(\text{shear})}, \quad h_1^{(\text{comp})} = \sqrt{3} h_1^{(\text{shear})}, \quad b^{(\text{comp})} = \sqrt{3} b^{(\text{shear})}, \\
g_1^{(\text{comp})} = \sqrt{3} g_1^{(\text{shear})}, \quad g_2^{(\text{comp})} = \sqrt{3} g_2^{(\text{shear})}, \quad S_{2i}^{(\text{comp})} = \sqrt{3} S_{2i}^{(\text{shear})}, \\
h_2^{(\text{comp})} = \sqrt{3} h_2^{(\text{shear})}, \quad l_1^{(\text{comp})} = \sqrt{3} l_1^{(\text{shear})}, \quad l_2^{(\text{comp})} = \sqrt{3} l_2^{(\text{shear})}, \\
\gamma^{(\text{comp})} = \sqrt{3} \gamma^{(\text{shear})}, \quad \dot{\epsilon}_r = \frac{1}{\sqrt{3}} \nu_r.
\end{array} \right\} \quad (8.46)$$

Further, to convert the temperature dependence parameters for the Young's modulus E to those for the shear modulus G , we use the standard relations

$$G_0 = \frac{E_0}{2(1 + \nu_{\text{poi}})}, \quad M = \frac{M_E}{2(1 + \nu_{\text{poi}})}, \quad (8.47)$$

with ν_{poi} assumed to be temperature-independent in the temperature range under consideration.

The material parameters for the three-dimensional theory that were determined by following the procedure described in this Appendix are listed for PMMA, PC, and Zeonex in Table 1.

Table 1: Material parameters for PMMA, PC and Zeonex

Parameter	PMMA	PC	Zeonex-690R
ϑ_g (K)	388	418	408
ρ (kg m ⁻³)	1200	1200	1010
α (K ⁻¹)	7×10^{-5}	6.5×10^{-5}	7×10^{-5}
G_0 (MPa)	296	638	482
M (MPa K ⁻¹)	10	0.74	0.16
ν_{poi}	0.35	0.37	0.40
X (MPa K ⁻¹)	9.4	1.5	0.7
γ	34.6	26.0	6.92
α_p	0.2	0.116	0.116
ν_0 (s ⁻¹)	2×10^{16}	2.1×10^{16}	3.2×10^{11}
m	0.218	0.08	0.16
Q (J)	1.81×10^{-19}	1.46×10^{-19}	1.81×10^{-19}
V (m ³)	3.655×10^{-28}	2.95×10^{-28}	1.97×10^{-27}
S_{1i} (MPa)	0	0	0
h_1	70	58	173
b (MPa)	5850	5850	5850
g_1	-4.92	-5.66	-16.17
g_2 (K ⁻¹)	0.0318	0.0381	0.0693
φ_i	0	0	0
φ_r	1.0×10^{-4}	6.6×10^{-4}	7.2×10^{-4}
k (K)	0.2	0.16	0.16
r	0.59	0.25	0.24
s	0.050	0.010	0.045
ν_r (s ⁻¹)	5.2×10^{-4}	5.2×10^{-4}	5.2×10^{-4}
n (K)	1.0	0.5	1.6
S_{2i} (MPa)	0	0	0
h_2	0	0.12	3.6
l_1 (MPa)	0	300	75
l_2 (MPa K ⁻¹)	0	0.35	0.16
μ_0 (MPa)	0.2	4.0	3.0
N (MPa K ⁻¹)	20.0×10^{-2}	11.4×10^{-2}	6.2×10^{-2}
I_m	5.5	7.8	6.2
c_0 (J kg ⁻¹ K ⁻¹)	1710	1630	2120
c_1 (J kg ⁻¹ K ⁻²)	4.1	3.6	8
κ_0 (Watt m ⁻¹ K ⁻¹)	0.190	0.187	0.467
κ_1	0.22	0.22	0.46
ω	0.65	0.8	0.8

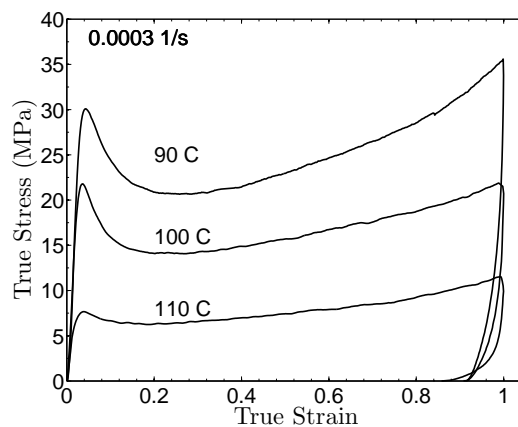
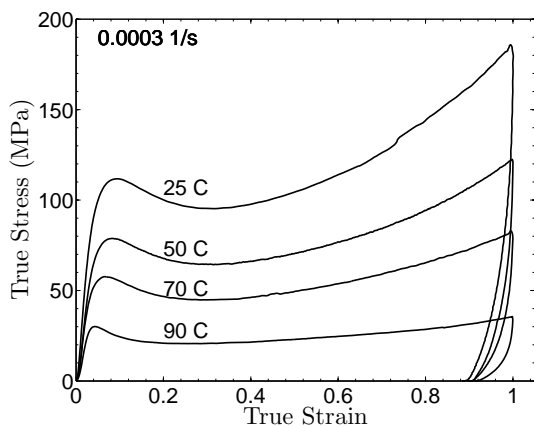


Figure 1: Stress-strain curves in simple compression for PMMA at various temperatures ranging from 25 C to 110 C, at a strain rate of $3 \times 10^{-4} \text{ s}^{-1}$. Note change in scale for the stress axis between the two figures.

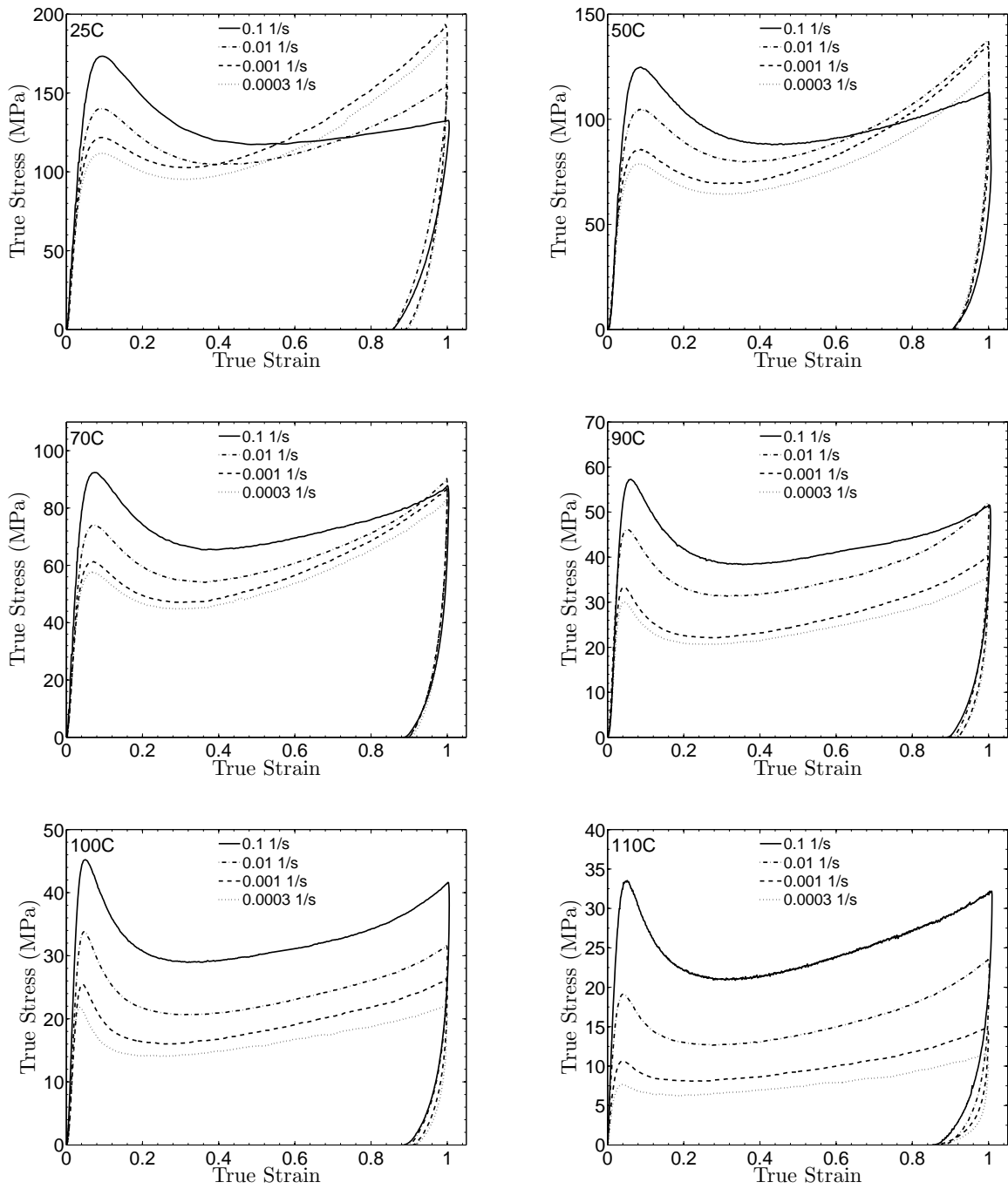


Figure 2: Stress-strain curves in simple compression for PMMA at strain rates of 3×10^{-4} , 10^{-3} , 10^{-2} , 10^{-1} s^{-1} , and temperatures of 25 C, 50 C, 70 C, 90 C, 100 C, and 110 C. Note change in scale for the stress axis between the various figures.

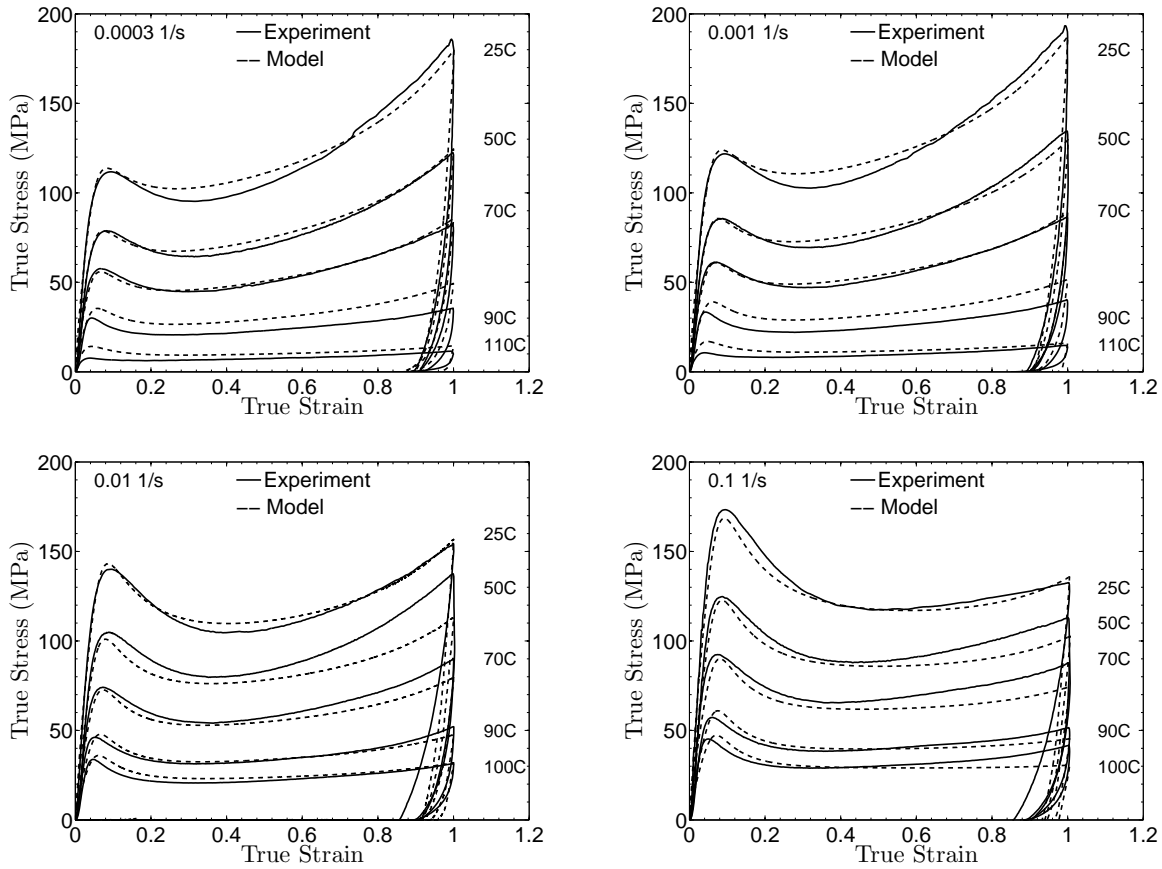


Figure 3: Fit of the constitutive model to the experimental stress-strain curves for PMMA at various temperatures ranging from 25 C to 110 C, and strain rates ranging from 3×10^{-4} to 10^{-1} s^{-1} . The experimental data is plotted as solid lines, while the fit is shown as dashed lines.

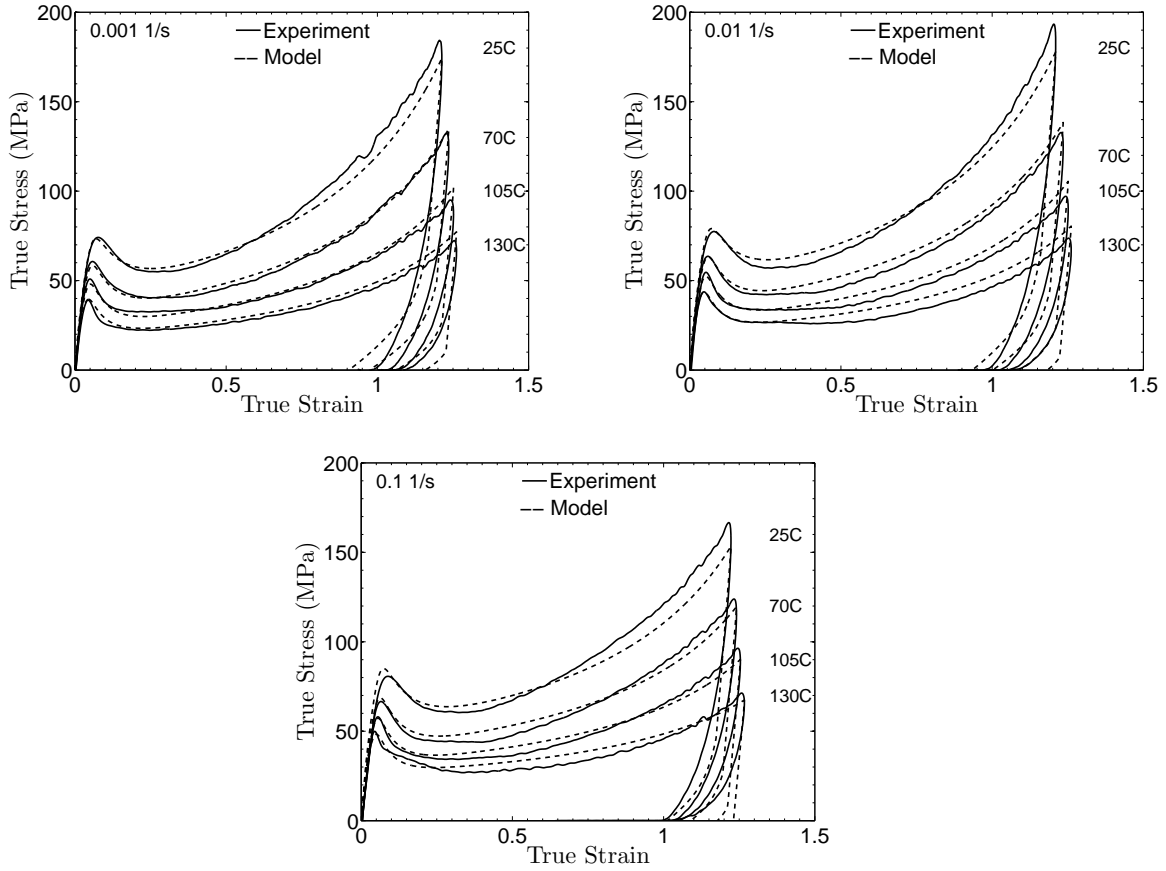


Figure 4: Fit of the constitutive model to the experimental stress-strain curves for PC at various temperatures ranging from 25 C to 130 C, and strain rates ranging from 10^{-3} to 10^{-1} s^{-1} . The experimental data is plotted as solid lines, while the fit is shown as dashed lines.

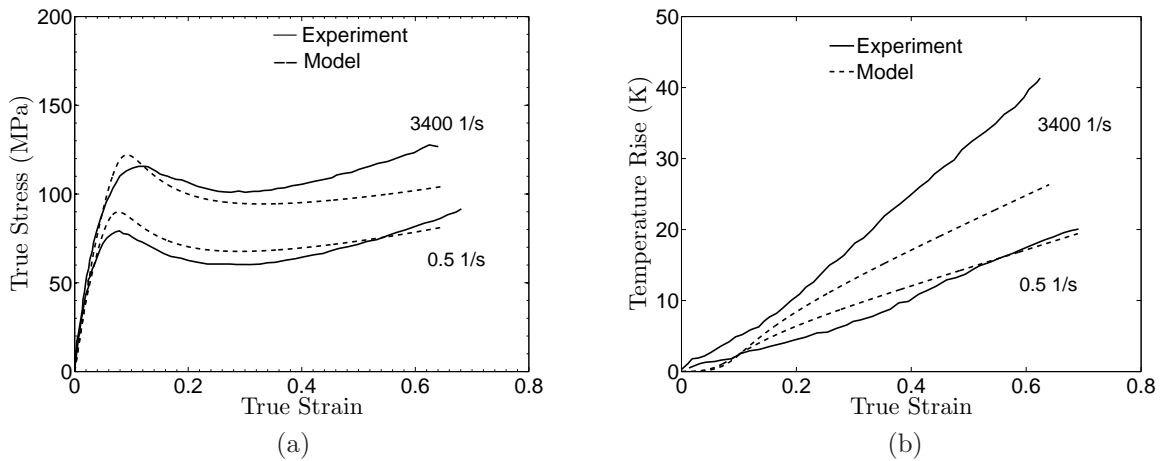


Figure 5: (a) Fit of the constitutive model to the high strain rate experimental stress-strain curves for PC at rates of 0.5 s^{-1} and 3400 s^{-1} , at an initial temperature of 25 C. (b) The corresponding rise in the surface temperature of the compression specimens. The experimental data (from Garg et al., 2008) is plotted as solid lines, while the fit is shown as dashed lines.

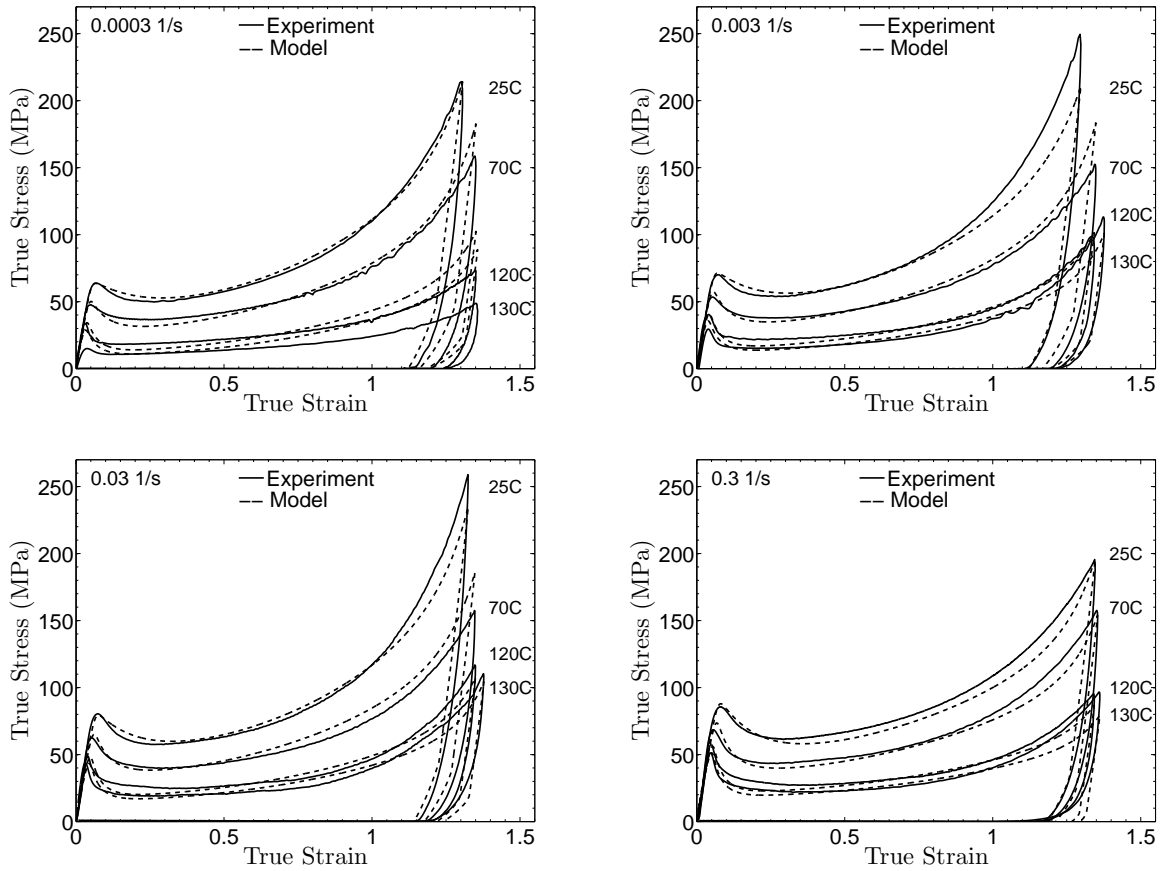
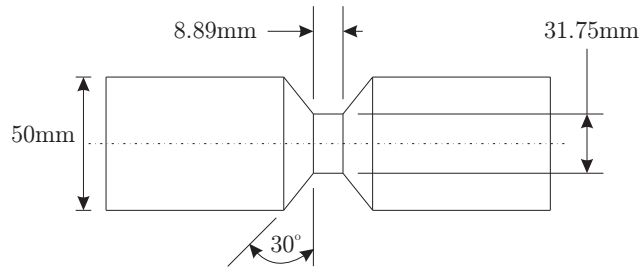
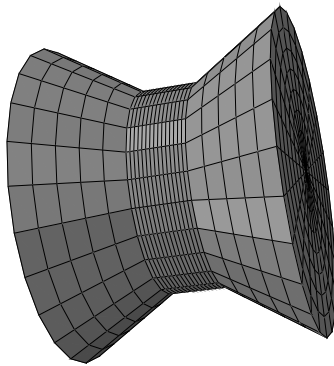


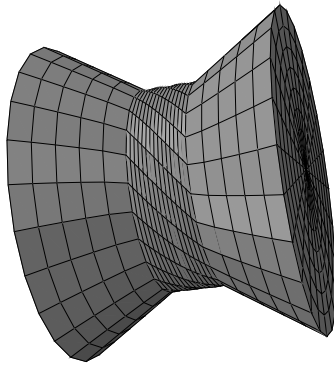
Figure 6: Fit of the constitutive model to the experimental stress-strain curves for Zeonex-690R at various temperatures ranging from 25 C to 130 C, and strain rates ranging from 3×10^{-4} to $3 \times 10^{-1} \text{ s}^{-1}$. The experimental data is plotted as solid lines, while the fit is shown as dashed lines.



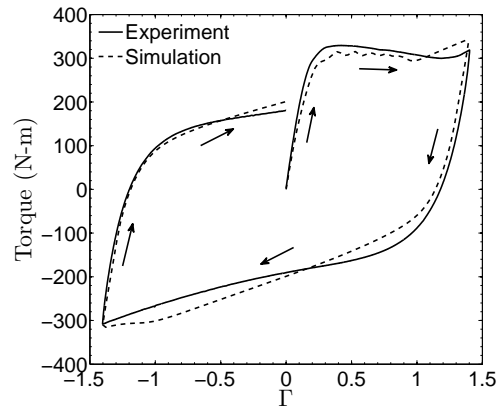
(a)



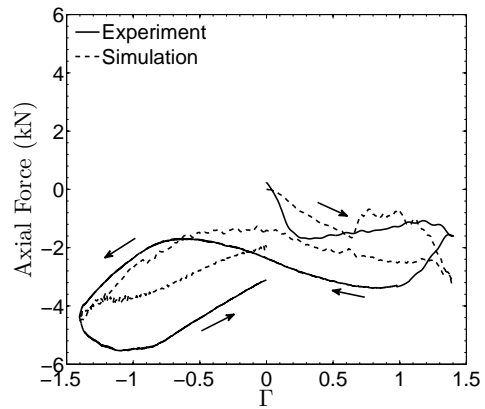
(b)



(c)



(d)



(e)

Figure 7: (a) Geometry of torsion specimen. (b) Undeformed finite element mesh for the torsion simulation. (c) Deformed finite element mesh at a surface shear strain of $\Gamma = 1.4$. (d) Torque versus surface shear-strain response for PC under reversed fixed-end torsion. (e) Axial-force versus surface shear-strain.

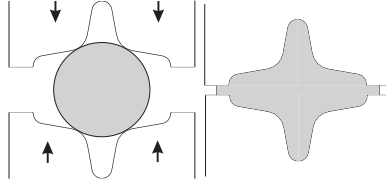


Figure 8: Schematic of the plane-strain cruciform-forging experiment.

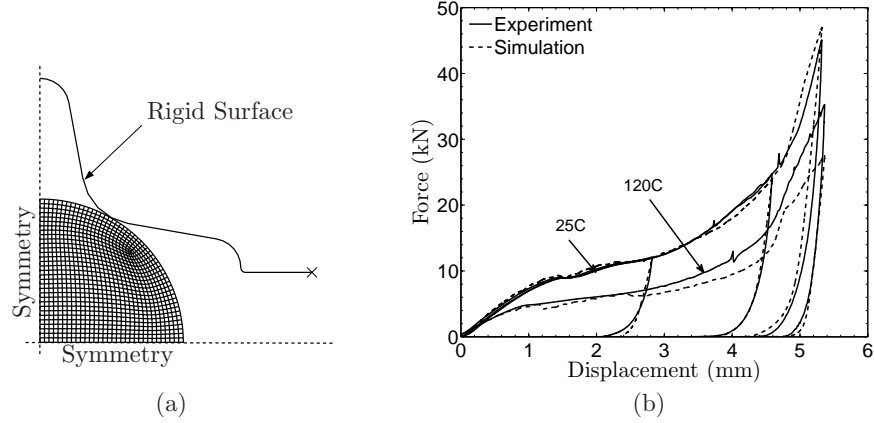


Figure 9: (a) Quarter-symmetry finite element mesh for the workpiece and the rigid surface used in the plane-strain cruciform-forging simulations for PC. (b) Comparison of numerically-predicted and experimentally-measured force-displacement curves for forgings at 25 C and 120 C.

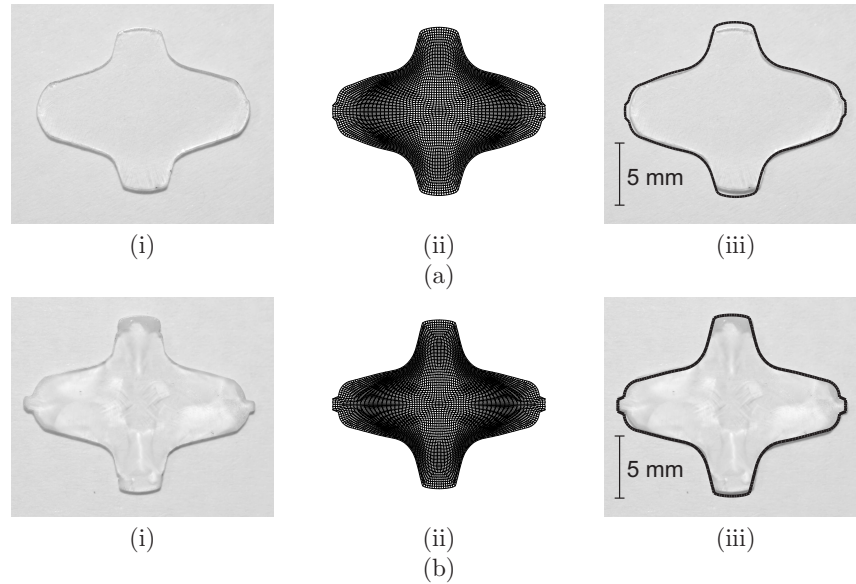


Figure 10: Comparison of numerically-predicted and experimentally-measured unloaded deformed shapes for the cruciform forging. (a) For a forging at 25 C at a die-displacement of 5.4 mm. (b) For a forging at 120 C at a die-displacement of 5.4 mm. (i) experimental macrographs; (ii) deformed meshes; and (iii) outlines of simulated shapes (thick black lines) superimposed over the experimentally-measured shapes.

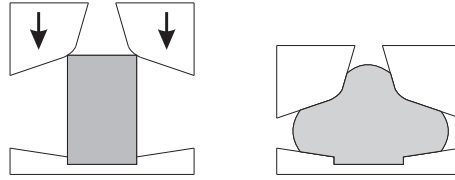


Figure 11: Schematic of the axi-symmetric forging experiment.

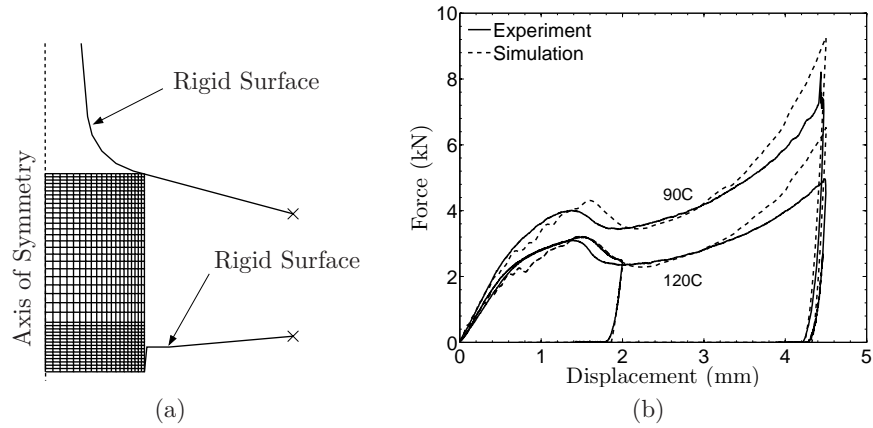


Figure 12: (a) Half-symmetry finite element mesh for the workpiece and the rigid surfaces used in the axi-symmetric cruciform-forging simulations for Zeonex. (b) Comparison of numerically-predicted and experimentally-measured force-displacement curves for forgings at 90 C and 120 C.

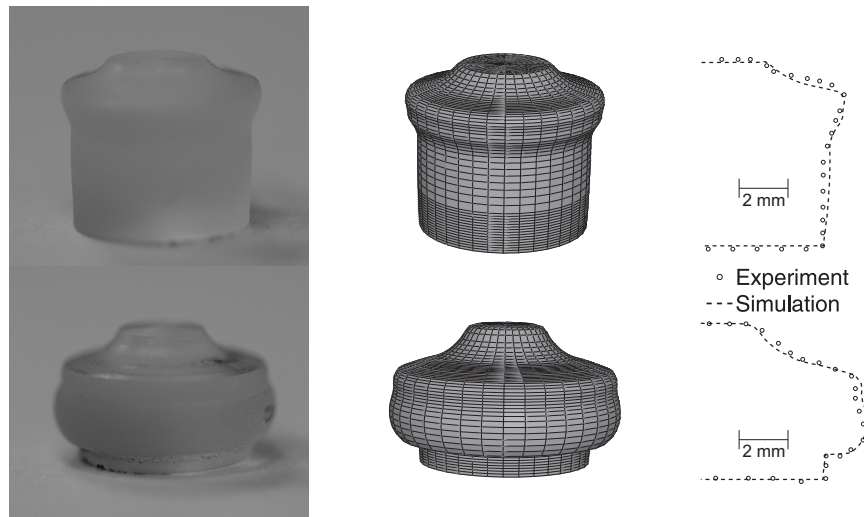


Figure 13: Comparison of numerically-predicted and experimentally-measured unloaded deformed shapes for the axi-symmetric forgings at 120 C after die displacements of 2 mm (top) and 4.5 mm (bottom).

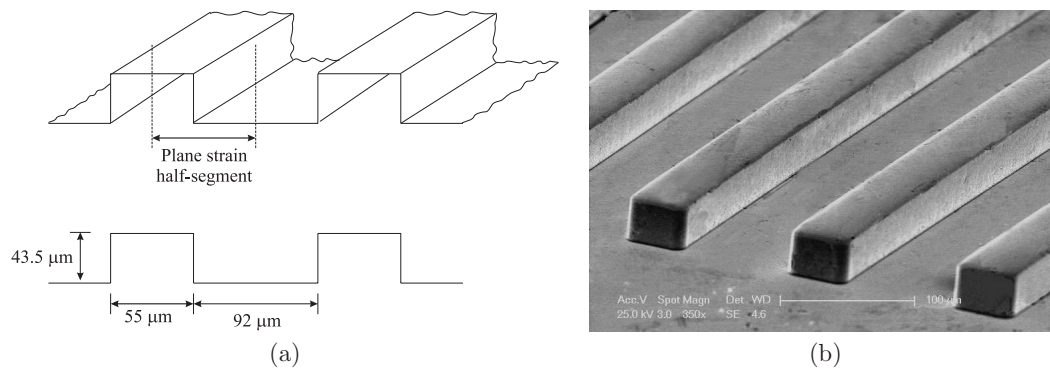


Figure 14: (a) Schematic of plane strain tool (not to scale). (b) SEM image of the metallic glass tool.

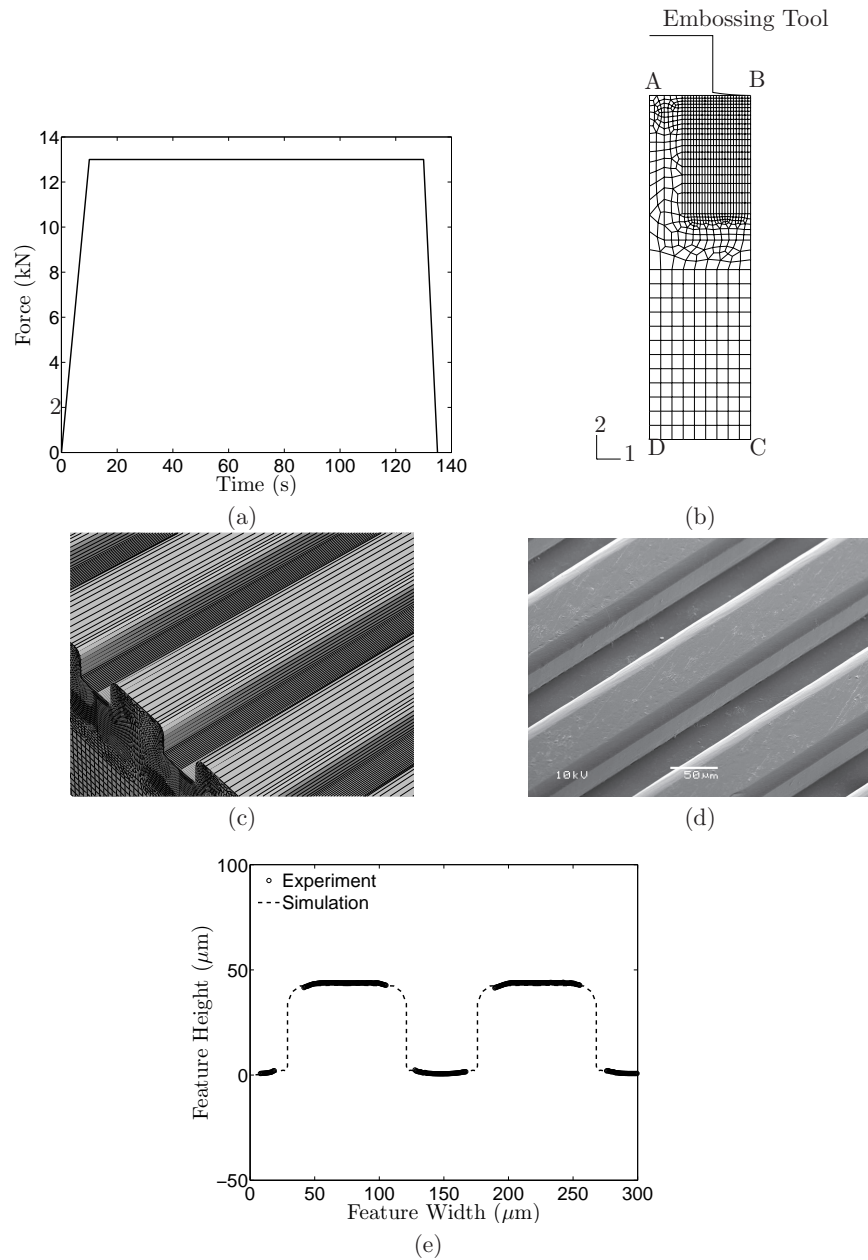


Figure 15: (a) The micro-hot-embossing was carried out at 130 C under load control; the process force history is shown. (b) Finite element mesh for a plane strain simulation showing the meshed substrate and the tool modeled as a rigid surface. The displacement boundary conditions on the portions AD and BC of the mesh boundary are $u_1 = 0$, while on the portion CD of the mesh, $u_1 = u_2 = 0$ are prescribed. (c) Predicted deformed shape. (d) SEM image of the micro-channels embossed in Zeonex. (e) Comparison of numerically-predicted channel profile (dashed line) with corresponding profilometer measurements.

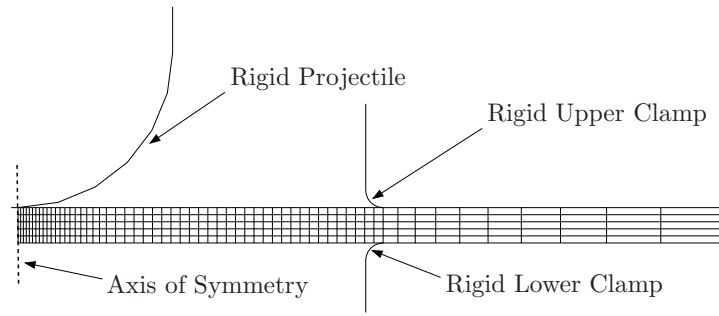


Figure 16: Finite element mesh used in the thermo-mechanically-coupled analysis of the plate impact experiment.

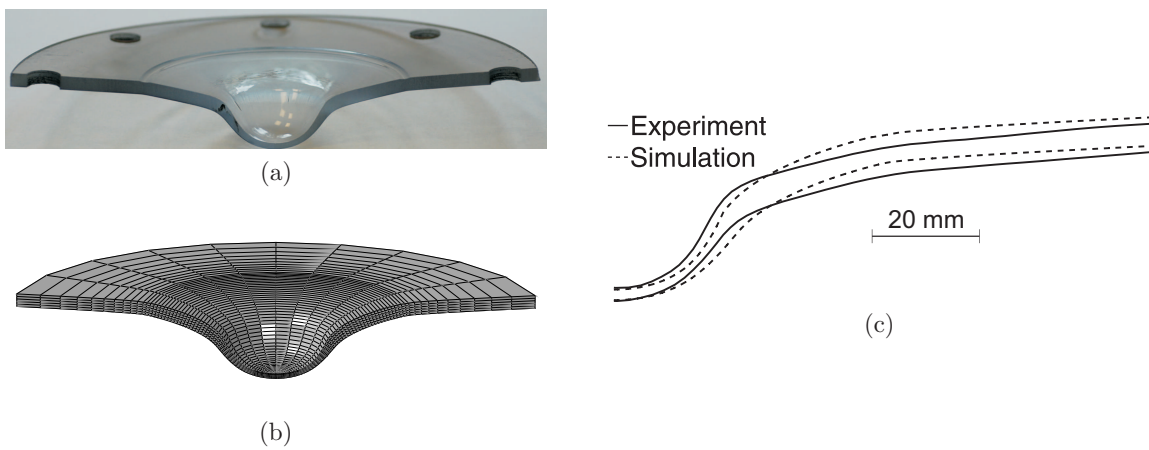


Figure 17: (a) Final shape of the impacted plate from the experiment. (b) Corresponding numerical prediction. (c) Comparison of traced surface profile of the specimen after impact with the numerically-calculated profile.

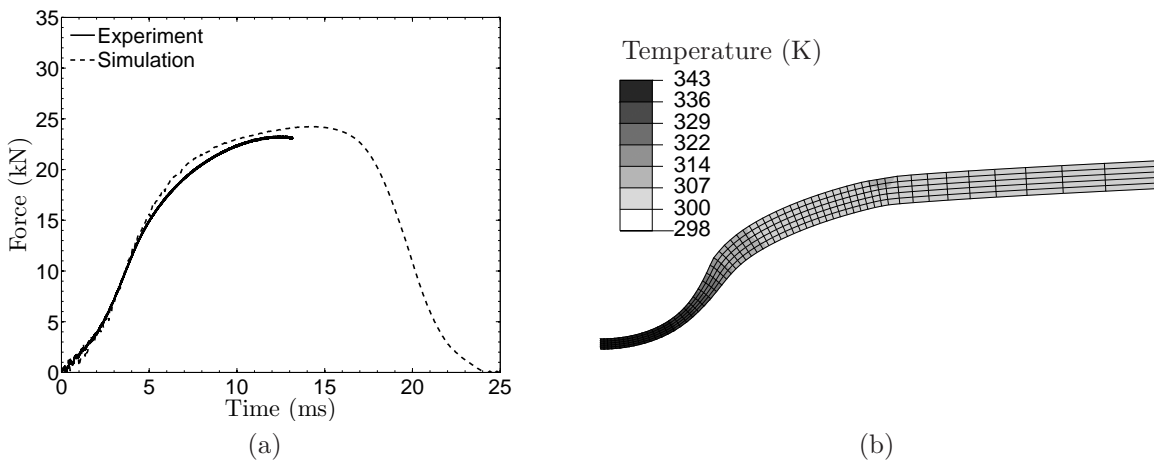


Figure 18: (a) Comparison of numerically-predicted and experimentally-measured reaction force versus time response for the projectile. (b) Contours of temperature in the deformed plate immediately after the impact.

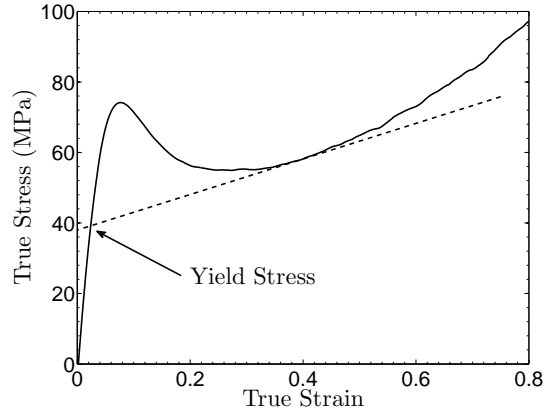


Figure 19: Schematic showing the “yield stress” defined as the intersection of the pre-peak stress-strain curve with the back-extrapolated tangent to the stress-strain curve at a strain of 0.4.

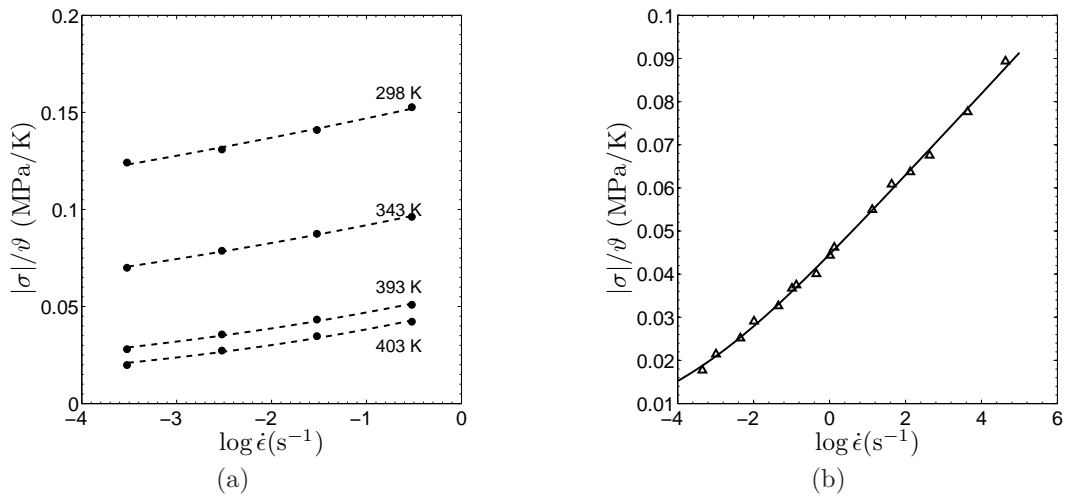


Figure 20: (a) Ratio of compressive yield stress to temperature as a function of logarithm of strain rate. The data plotted as bullets (●) are the yield stress values estimated from the compression experiments, and the dashed lines are estimated isotherms. (b) Master curve constructed at 408K by shifting the yield stress data. The shifted experimental data is plotted as triangles (△), and the solid line indicates a fit of flow function to the master curve.

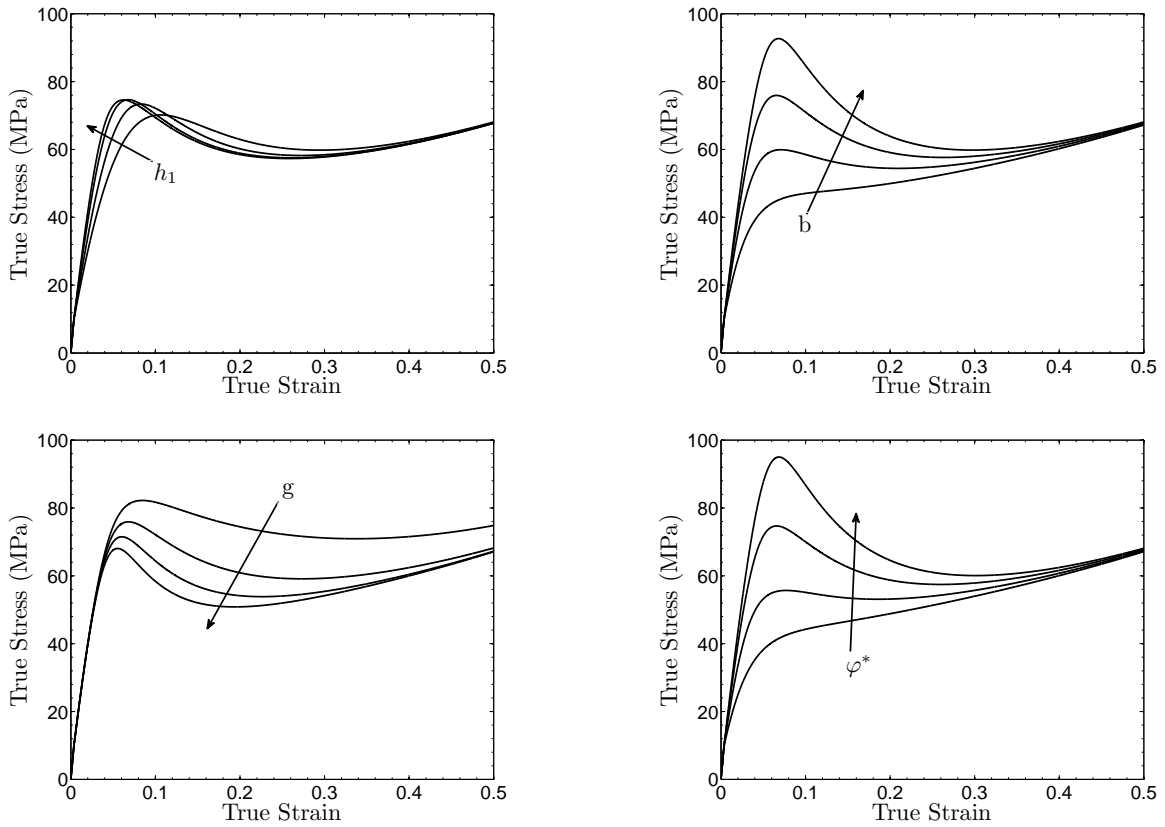


Figure 21: Schematics of the effects of the material parameters $\{h_1, b, g, \varphi^*\}$ on the shape of the yield-peak. Arrows indicate changes as the values of the respective parameters are increased.

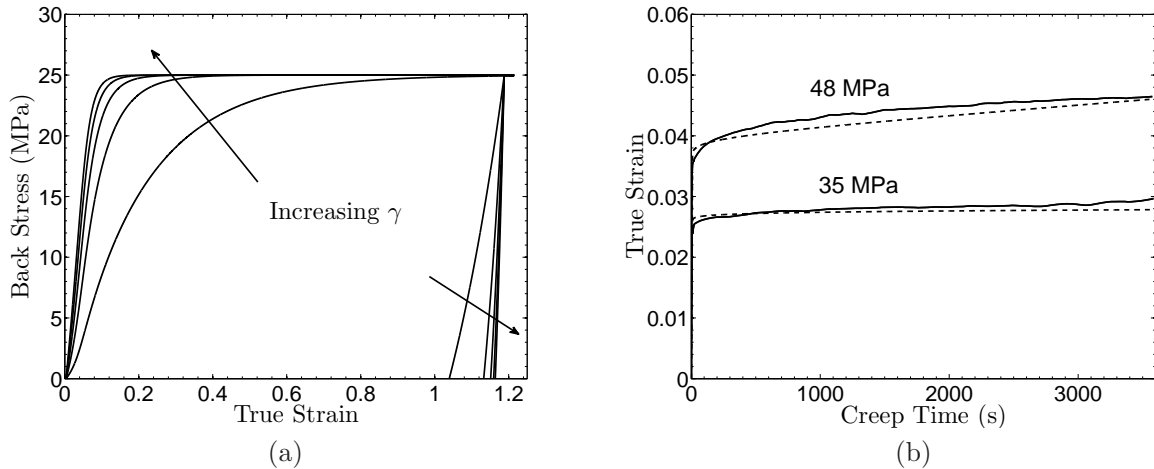


Figure 22: (a) The dependence of the evolution of back-stress on the material parameter γ : effect of sequentially doubling the material parameter γ from 5 to 160 on the back-stress for a constant ratio of B/γ . (b) Creep test results under simple compression at two stress levels below the yield-peak (solid lines), together with one-dimensional MATLAB simulations (dashed lines).

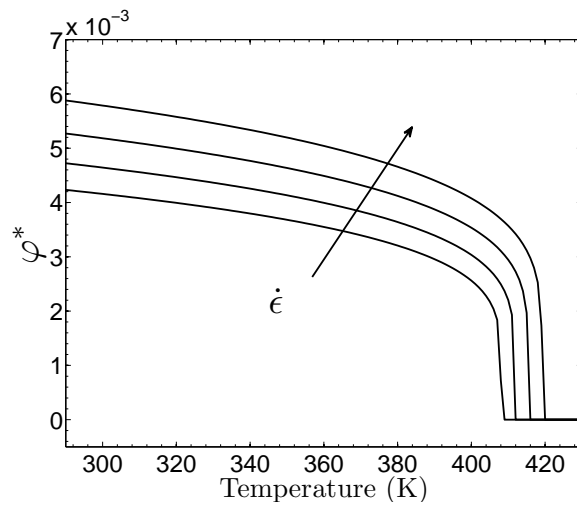


Figure 23: Temperature and rate dependance of φ^* . The arrow indicates an increase in the strain rate.